

Coordination of Contractility, Adhesion and Flow in Migrating
Physarum Amoebae

Owen L. Lewis^{1,†}, Shun Zhang², Robert D. Guy³, and Juan C. del Álamo²

¹Department of Mathematics, University of Utah

²Mechanical and Aerospace Engineering Department, University of California San Diego

³Department of Mathematics, University of California Davis

[†]Corresponding Author: olewis@math.utah.edu

March 30, 2015

Abstract

This work examines the relationship between spatiotemporal coordination of intracellular flow and traction stress and the speed of amoeboid locomotion of microplasmidia of *Physarum polycephalum*. We simultaneously perform particle image velocimetry and traction stress microscopy to measure the velocity of cytoplasmic flow and the stresses applied to the substrate by migrating *physarum* microamoebae. In parallel, we develop a mathematical model of a motile cell which includes forces from the viscous cytosol, a poro-elastic, contractile cytoskeleton and adhesive interactions with the substrate. Our experiments show that flow and traction stress exhibit back-to-front directed waves with a distinct phase difference. The model demonstrates that the direction and speed of locomotion is determined by this coordination between contraction, flow, and adhesion. Using the model, we identify forms of coordination that generate model predictions consistent with experiments. We demonstrate that this coordination produces near optimal migration speed and is insensitive to heterogeneity in substrate adhesiveness. While it is generally thought that amoeboid motility is robust to changes in extracellular geometry and the nature of extracellular adhesion, our results demonstrate that coordination of adhesive forces is essential to producing robust migration.

Keywords: amoeboid motility, traction force microscopy, cytoplasmic streaming, cell locomotion, particle image velocimetry

1 Introduction

Cell migration plays a critical role in a wide variety of biological processes, including morphogenesis, wound healing and the immune response. Amoeboid motility is a fast type of cell migration defined by large shape changes as the cell extends and retracts various pseudopodia and blebs [46]. These extensions are driven by the interplay between substrate adhesion, the polymerization of filamentous actin and the pressure driven flow of cytoplasm [39]. Research on amoeboid motility has recently intensified in part because this migration mode is robust to changes in the extracellular matrix and the specific molecular nature of the cell-matrix adhesions [35, 17]. That is to say, amoeboid cells are able to cross barriers, move through confined channels, or squeeze through 3-D matrices by contracting and pushing-off the surrounding environment. This versatility has also spurred the exploratory design of bio-inspired millimetric robots made of active self-oscillating hydrogels [36]. Despite the vast existing knowledge about the biological and molecular processes involved in cell migration, our understanding of the underlying mechanical processes is still rather phenomenological. In particular, the coordination of contractility, adhesion and flow of cytoplasmic material that enables pseudopod extension is not fully understood. In fact, it is not even clear if coordination of these processes is necessary for motility in all scenarios [35].

This work investigates the coordination of cellular contractile force, substrate adhesion and cytoplasmic flow in migrating amoebae of the slime mold *Physarum polycephalum*. *Physarum* plasmodia generate a periodic flow of cytoplasm (known as shuttle streaming) through a tubular network. This flow is driven by pressure gradients created by contraction of the actomyosin network within the plasmodium [30, 13, 41]. Small-scale *physarum* amoebae ($\sim 100\mu\text{m}$ in length) can exhibit a similar behavior where a rhythmic flow of cytoplasm moves back and forth along the centerline of a roughly tadpole shaped cell. The onset of this behavior has been observed to coincide with a drastic increase in the locomotion speed of growing *physarum* [43]. Larger scale plasmodia ($l \sim 500\mu\text{m}$) can develop more complex morphologies including chains of round contractile heads connected by relatively inert tubes, as shown by Rieu et al in a companion paper [51].

Due to the relatively large scale of the organism, Particle Image Velocimetry (PIV, [44]) experiments allow researchers to measure the intracellular fluid velocity in *physarum* amoebae using cell organelles as flow tracers. The periodic waves of cytoplasmic streaming in tadpole shaped cells

have been well characterized by PIV and it has been argued that the traveling-wave nature of the intracellular flow is responsible for generating directed motility [22]. However, a purely hydrodynamic explanation of *physarum* amoeboid motility does not address the transmission of traction stress to the underlying substrate, which is ultimately necessary for cellular migration to take place. It is unclear if passive, uncoordinated cell-substrate interactions are sufficient for *physarum* plasmodia to effectively “flow” across a substrate. Alternately, the motility of *physarum* plasmodium might depend upon cell-substrate adhesion being dynamically coordinated relative to the stresses generated by the flow. It is known that substrate bound structures are mechanically linked to the actomyosin network within the plasmodium [16]. However, the precise nature of these structures is not well studied, and there currently exists no quantitative description of the stresses which the cell exerts on the substrate as it migrates, nor how these stresses are correlated to the cytoplasmic flow.

To answer these questions, we concurrently perform Traction Force Microscopy (TFM) and PIV measurements on migrating *physarum* amoebae. In the past, TFM has been used to study the adhesive forces that enact locomotion of a diverse array of unicellular and multicellular organisms ranging from a few microns to a few centimeters in size [45, 24, 42, 29]. In conjunction with these experiments, we develop a computational model for migrating *physarum* amoebae based on a modified Immersed Boundary (IB) [50]. The model accounts for hydrodynamic effects, elastic forces within the cell interior, and adhesive coupling of the cytoskeleton to the substrate. We use the model to examine how cytoskeletal contraction, cytosolic flow, and cell-substrate adhesion work together to generate cell locomotion.

Our measurements show that traction stresses in migrating *physarum* amoebae are mainly distributed along the cell periphery forming an inward contractile pattern. These stresses are spatiotemporally modulated to establish a rhythmic contraction wave that travels in the direction of cell migration. The contractile wave has the same time period as the intracellular flow waves previously described, and a phase lag of approximately 1/3 of a cycle. These spatiotemporal flow and stress patterns are reproduced by the numerical simulations using an idealized model of adhesion. We apply this adhesion model to investigate the strength of adhesion and its coordination *relative* to the rhythmic flow of cytoplasm. Specific coordination patterns are identified which are consistent with experimental data. These parameters are seen to be optimal in that they (nearly) maximize migration velocity of the model cell for a given strength of actomyosin contraction. Finally, we perform numerical simulations of the model cell crawling across randomly heterogeneous substrates and show that the speed of migration is only mildly perturbed. These simulations imply that the proposed model of motility is robust to perturbations of adhesiveness of the extracellular substrate.

2 Experimental Materials and Methods

This section summarizes the cell culture, microscopy and analysis methods employed to prepare migrating *physarum* microamoebae, and to jointly measure the intracellular flows and traction forces generated by these amoebae while migrating. A more exhaustive description of these methods can be found in the Supplementary Information. *Physarum* plasmodia were obtained from a generous gift by Toshiyuki Nakagaki (Research Institute for Electronic Science, Hokkaido University) and cultured as previously described [22]. Small portions of area $\sim 0.2 \times 0.2 \text{ mm}^2$ were cut from the parent plasmodia to produce migrating amoebae, which were transferred to collagen-coated polyacrylamide (PA) gels embedded with fluorescent beads. The PA gels were prepared as previously described [32]. We kept the PA gel humidified throughout the experiment and flattened the amoe-

bae to facilitate intracellular flow visualization by placing an agarose cap on top of the PA gel containing the specimen.

Using an inverted microscope, we simultaneously acquired transmitted-light and fluorescence z-stack image sequences of the migrating *physarum* amoebae with time resolutions of 0.2 s and 12 s respectively. These data enabled us to jointly measure the intracellular flow and traction forces generated by the amoebae, which oscillate with a much slower period of ~ 100 sec [22].

Physarum's dense distribution of intracellular vesicles was exploited to determine intracellular streaming velocities from the transmitted light images using particle image velocimetry (PIV) [22, 44]. The raw image sequences were pre-processed for PIV by applying high-pass, band-pass and low-pass temporal filters, which allowed us to resolve the flow inside narrow channels (see Figure 2(a)). The resulting spatial resolution of the flow measurements was $6.5 \mu m$.

The three-dimensional deformation produced by *physarum* amoebae on the PA substrate was measured by tracking the displacements of the embedded fluorescent beads as described by del Álamo et al. [32]. From the measured deformation, we computed the traction stresses (see Figure 2(b)) and strain energy (see Figure 9) generated by the cells using Fourier TFM methods described elsewhere [42, 32]. The spatial resolution of these measurements was $13 \mu m$.

3 Mathematical Model

Our model of the cell incorporates the effects of intracellular liquid (cytosol), the solid internal cell structure (cytoskeleton), and interaction with the extracellular substrate (through adhesion) in a moving geometry defined by the cell membrane and underlying cortex (see Figure 1). The model is described by the balance of forces on three materials: the liquid cytosol, the porous elastic cytoskeleton, and the adhesive complexes which mechanically couple the cell interior to the substrate. The velocity of the viscous cytosol (\vec{u}_f) satisfies the forced Stokes equations. The fluid forces (viscosity and pressure) are balanced by body forces from the drag due to the internal cytoskeleton (\vec{f}_{drag}) and the elastic forces on the membrane/cortex which bounds the cell (\vec{f}_{mem}). The forces acting on the cytoskeleton are the elastic forces due to deformation (\vec{F}_e), an active contractile force due to myosin molecular motors in the actin network (\vec{F}_a), drag due to the cytosol (\vec{F}_{drag}), forces due to adhesions to the substrate (\vec{F}_{adh}), and forces generated by attachment of the cytoskeletal network to the surrounding membrane/cortex ($\vec{F}_{\text{net}}^{\text{attach}}$). Finally, the adhesion complexes are subject to forces applied by the external substrate (\vec{F}_{subs}), balanced by the forces which the complexes apply to the internal cytoskeleton. The system of equations which describe these force balances is

$$\mu \Delta \vec{u}_f - \nabla p + \vec{f}_{\text{drag}} + \vec{f}_{\text{mem}} = 0, \quad (1)$$

$$\nabla \cdot \vec{u}_f = 0, \quad (2)$$

$$\vec{F}_e + \vec{F}_a + \vec{F}_{\text{drag}} + \vec{F}_{\text{adh}} + \vec{F}_{\text{net}}^{\text{attach}} = 0, \quad (3)$$

$$\vec{F}_{\text{subs}} - \vec{F}_{\text{adh}} = 0. \quad (4)$$

These equations effectively describe the cell interior as an actively contractile poro-elastic network. A similar model (with an additional description of chemical kinetics) has been used to investigate symmetry breaking and the onset of contractile waves in *physarum* microplasmidia [21, 20]. For a description of how we compute these forces and the material parameters, see [34], as well as Supplemental Section S.2.

The active contractile force (\vec{F}_a) drives the deformation of the cell and the flow of cytosol. We

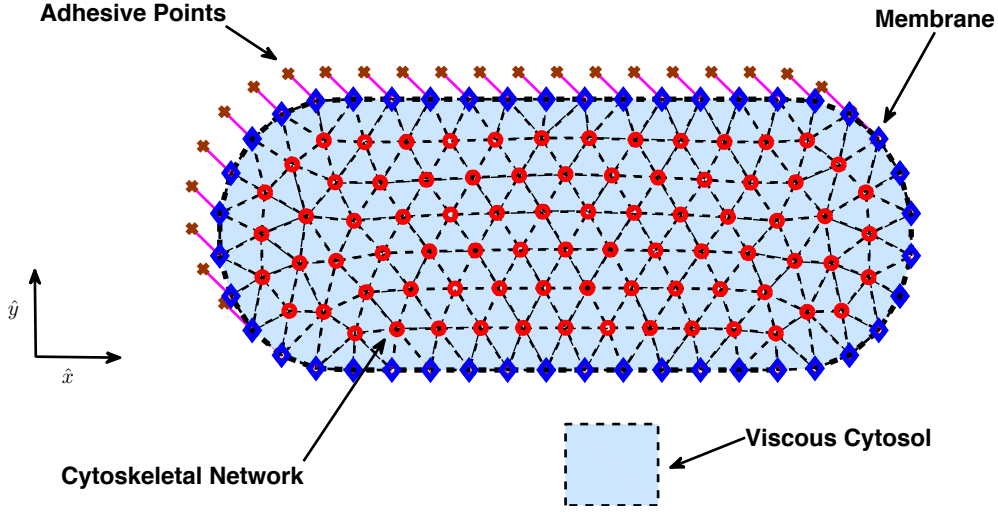


Figure 1: A schematic of our computational model of a *physisarum* plasmodium. Cytoskeletal network points are shown as red circles. Membrane points are shown as blue diamonds. Adhesive points are illustrated as brown exes. Viscous cytosol that permeates the porous media is illustrated as light blue shading.

assume that this force is generated by a traveling wave of isotropic contractile *stress* with magnitude

$$\Sigma_a(x, t) = \frac{C}{2} \left(\cos \left(\frac{2\pi}{\ell_{\text{cont}}} x - \frac{2\pi}{T} t \right) + 1 \right), \quad (5)$$

where C is the maximum contractile stress, ℓ_{cont} is the wavelength, and T is the period. The spatial variable x is the longitudinal body coordinate of the cell. The wave travels along the body (from posterior to anterior) with wavespeed ℓ_{cont}/T . We assume that the resulting wave of cell shape deformation is directly correlated with the underlying cytoskeletal contraction and choose $\ell_{\text{cont}} = 1600 \mu\text{m}$ (four body lengths) and $T = 100 \text{ sec}$, which is consistent with the wavelength and period of deformation reported in [22] and with our own experiments. Similarly, the value of C is chosen so that the resulting deformations of the model cell are on the same scale as those observed in experiments.

Many of the material parameters can be measured or estimated. Conversely, the precise nature of the proteins with which *physisarum* adheres to the substrate is not known, even if some candidates have been identified [26]. The period of the deformations observed in *physisarum* is long ($\sim 100 \text{ sec}$) compared to the timescale of the dynamics of a cell-substrate bond, and so we represent the dynamics of adhesion via a viscous drag law [23] of the form

$$\vec{F}_{\text{subs}} = -\zeta(x, t)\vec{U}_{\text{adh}}, \quad (6)$$

where \vec{U}_{adh} is the velocity of the adhesion complexes (relative to the substrate), and ζ is a viscous

interaction coefficient. In Section 4.5 we investigate an idealized ζ of the form

$$\zeta(x, t) = \frac{A}{2} \left(\cos \left(\frac{2\pi}{\ell_{\text{adh}}} x - \frac{2\pi}{T} t + \phi \right) + 1 \right) + \epsilon. \quad (7)$$

This choice of ζ is inspired by the observation that both the deformation of, and associated flow within *physarum* appear to propagate from the posterior to the anterior of the cell as a traveling wave (discussed in more detail in Section 4). The wavelength ℓ_{adh} and period T of the adhesion modulation are assumed to be the same as those of the contractile wave. The parameter ϕ represents the phase of the coordinated adhesion *relative* to the traveling wave of contraction strength (eq. (5)). The amplitude parameter A is a measure of the strength of active coordinated adhesion, and will often be referred to as the “coefficient of adhesion” in the following text. The parameter ϵ represents nonspecific adhesive interactions between the substrate and the basal surface of the cell. We report coefficient of adhesion in nondimensional units of $[A/\epsilon]$.

4 Results

4.1 Cell Behavior

Upon reaching an adequate size (approximately 100 μm across), we observe the cells elongate into a tadpole-like shape concurrent with the onset of a rhythmic, pulsating flow of cytosol. In most cases, this behavior is similar to that reported in [22], with waves of contraction and flow traveling from posterior to anterior along the long axis of the cell. We refer to these cells as “peristaltic.” We also observe a second mode of deformation which we call “amphistaltic” due to the fact that the front and rear contract and relax in an anti-phase manner. The amphistaltic amoeboid mode could be the precursor of the contractile dumbbells found by Rieu et al. in the companion paper [51]. Of the 21 cells we study, 10 of them clearly exhibit the peristaltic behavior, while 6 are amphistaltic. For an illustration of the difference between these modes, see Supplementary Information. Approximately 5 of the cells we observe do not obviously fall into the category of peristaltic or amphistaltic mode, and exhibit characteristics of each. The peristaltic mode appears to be stable on timescales of at least 1000 sec. After this, the cells migrated far enough to leave the observation window. In this work we focus only on the peristaltic cells due to the fact that they migrate approximately twice as fast as amphistaltic cells, and are consistent with the experiments of previous investigations [22].

In peristaltic cells, the cytoplasmic flow is primarily directed along the cell centerline from its anterior to its posterior end (hereafter referred to as the longitudinal or cell axis), and has a distinct period of 90 ± 12 sec (measured over 10 cells). A region of cytoplasmic flow directed forward develops at the cell rear. This pattern of forward flow becomes more prominent and travels along the cell axis toward the cell front. Eventually, a region of flow directed backwards emerges at the cell rear, and it also propagates toward the cell front, before the entire pattern repeats. Figure 2(a) shows three instantaneous measured velocity fields: a fully developed forward flow pattern, a fully developed backward directed flow pattern, and the final stages of the backward flow pattern, as a new forward flow begins at the posterior of the cell. The emergence of this periodic wave of back-and-forth flow is observed to coincide with a dramatic increase in the migration velocity of the cell [43].

The migration of the cell is necessarily accompanied by the application of traction stresses to the substrate. Figure 2(b) shows a sequence of the stresses applied to the substrate by *physarum* at three time points which are approximately those reported in Figure 2(a). There is a slight time difference between the images of (a) and (b) due to changing the imaging channel of the

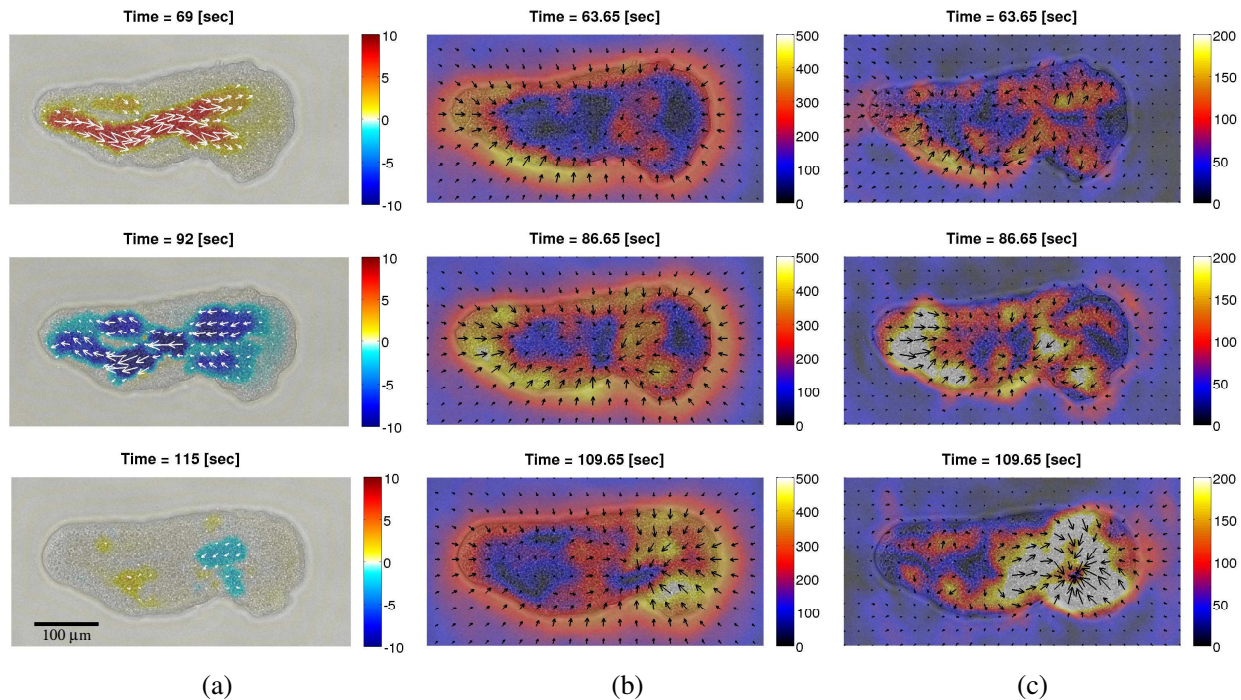


Figure 2: (a) Instantaneous intracellular flow observed in migrating *physarum*. Arrows indicate the direction of flow, colormap indicates the projection of flow velocity onto the cell axis [$\mu\text{m}/\text{sec}$]. (b) Instantaneous traction stresses exerted on the substrate. Arrows indicated the direction of traction stress, colormap indicates the magnitude [Pa]. (c) Traction stresses with the moving cortical average removed. Arrows indicate the direction of stresses, colormap indicates the magnitude [Pa]. All arrow fields are downsampled by a factor of 4 in each direction for visual clarity.

microscope from bright field to fluorescent field. Supplementary Movie 1 shows the joint time evolution of intracellular flow and traction stresses for the cell in Figure 2.

The dominant feature of this traction stress pattern is purely contractile, with the larger stresses distributed along the cell periphery. This behavior has been observed in other cell types, and it has been hypothesized that this effect is due to strong stresses associated with the cell cortex and directed out of the plane of the substrate [3]. Because our model only considers in-plane stress, we remove the average “cortical” stress from the measured stress field to compare with model predictions (See Supplemental Information). At each instant of time, the average traction stress field is compiled from the traction stresses recorded during the previous, current and following periods of the observed behavior. We then remove the average contractile stress from the instantaneous traction stress field, yielding the stress patterns shown in Figure 2(c). This procedure reveals loci of expansive and contractile stress that propagate from the posterior to the anterior. As the expansive locus leaves the front of the cell, a new one develops behind the contractile locus.

4.2 Comparison of Model Behavior

In this section, we illustrate the behavior of our model simulations and compare with experimental observations. All simulations were run with $\phi = 3\pi/2$ and $A = 100\epsilon$, respectively. In Sections 4.4 and 4.5 we justify this choice and consider other adhesion parameters. In Figure 3(a) we show instantaneous fluid velocity fields obtained from the model at time intervals analogous to Figure 2.

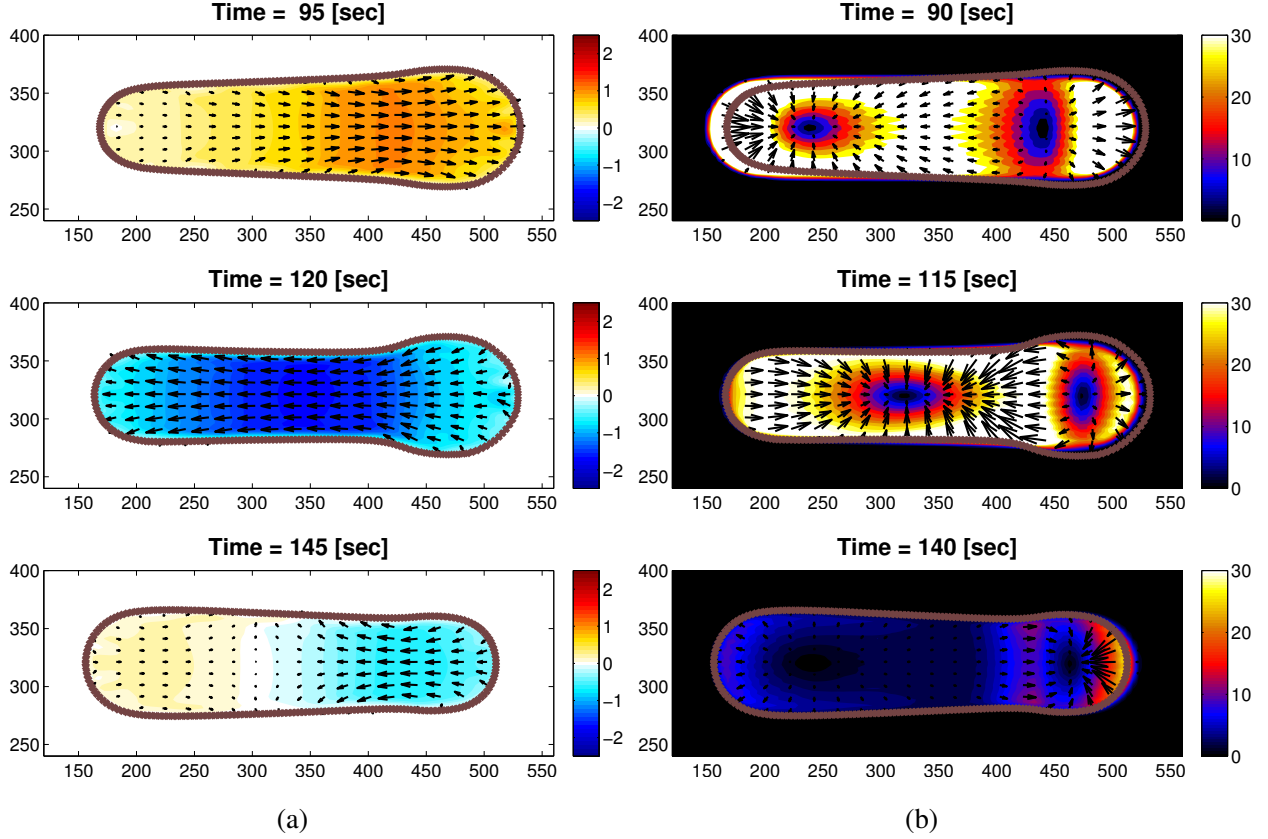


Figure 3: (a) Instantaneous intracellular flow computed in model cell. Arrows indicate the direction of flow, colormap indicates the projection of flow velocity onto the cell axis [$\mu\text{m}/\text{sec}$]. (b) Instantaneous traction stresses computed in model cell. Arrows indicate the direction of stress field, colormap indicates the magnitude of stress field [Pa]. Again, all arrow fields are downsampled by a factor of 4 in each direction for visual clarity.

The three panels illustrate a fully developed forward flow, a fully developed region of backward flow, and the onset of a forward flow pattern at the posterior of the cell (Supplementary Movie 2 shows the time-resolved animation). Qualitatively, they are very similar to the behavior shown in Figure 2(a). In Figure 3(b) we provide illustrations of traction stress fields (\vec{F}_{trac}) generated by our model cell during the same simulation shown in Figure 3(a). The time points shown are offset from those in Figure 3(a) for a more direct comparison with experiments. The three panels show the forward propagation of a contractile locus of stress through the cell body, as well as a locus of expansive stress that exits the anterior of the cell before a weaker one emerges at the posterior (Supplementary Movie 3 shows the time-resolved animation). In this regard, the model again reproduces the qualitative behavior observed in live *physarum*.

To further analyze the flow patterns that we observe (or our model predicts), we generate kymographs of the measured (or calculated) longitudinal flow averaged over each lateral cross section of the cell,

$$\bar{U}(x, t) = \frac{\int_{\Omega_c} \vec{u}_f \cdot \hat{x} dy}{\int_{\Omega_c} dy}, \quad (8)$$

where Ω_c denotes the interior of the cell, x is the longitudinal coordinate, y is the coordinate

orthogonal to the longitudinal axis, and \hat{x} is unit vector oriented towards the anterior of the cell. Similarly, we compare kymographs of the observed and measured traction stresses by defining

$$\bar{S}(x, t) = \frac{\int_{\Omega_c} \vec{F}_{\text{trac}} \cdot \hat{x} dy}{\int_{\Omega_c} dy}, \quad (9)$$

which measures the average traction stress *in the direction of motion* at each cross section of the cell body.

Figure 4 shows experimental measurements of \bar{U} , together with results for the model cell. For

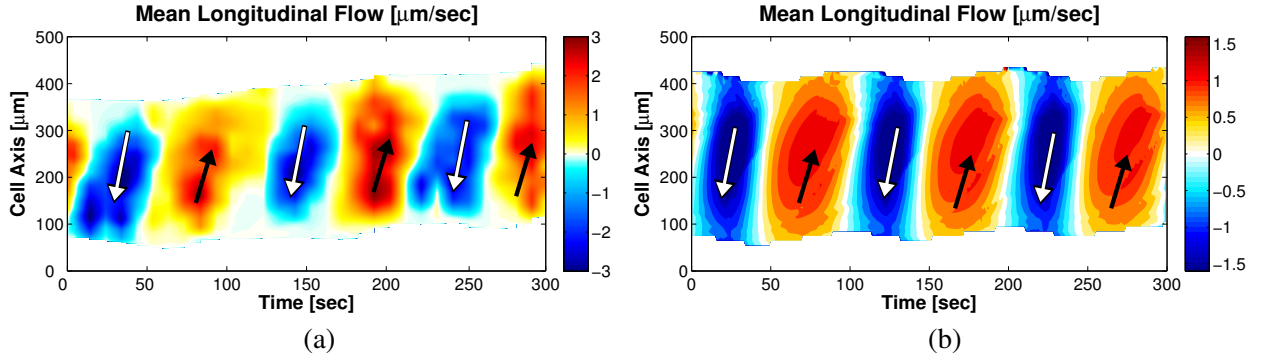


Figure 4: Kymographs of mean longitudinal flow \bar{U} . (a) Data recorded in migrating physarum. (b) Values predicted by model simulation. Filled arrows indicate flow directed forward. Open arrows indicate regions of backward flow.

both our experiments and simulations, we observe flows in good agreement with those reported previously [22]. A periodic pattern is clearly evident, where regions of forward and rearward flow are generated at the back of the cell, and quickly propagate toward the front in an approximately linear fashion. We refer to this pattern as a “phase wave,” and to its propagation speed as the “phase velocity”, c_ϕ . In previous experiments this phase velocity was reported as $c_\phi = 12 \pm 1 \mu\text{m}/\text{sec}$ [22]. Here, we measure higher phase velocities, $c_\phi = 23.8 \pm 12.0 \mu\text{m}/\text{sec}$ across our experiments, and our model predicts $24 \leq c_\phi \leq 38 \mu\text{m}/\text{sec}$ (See Supplemental Information).

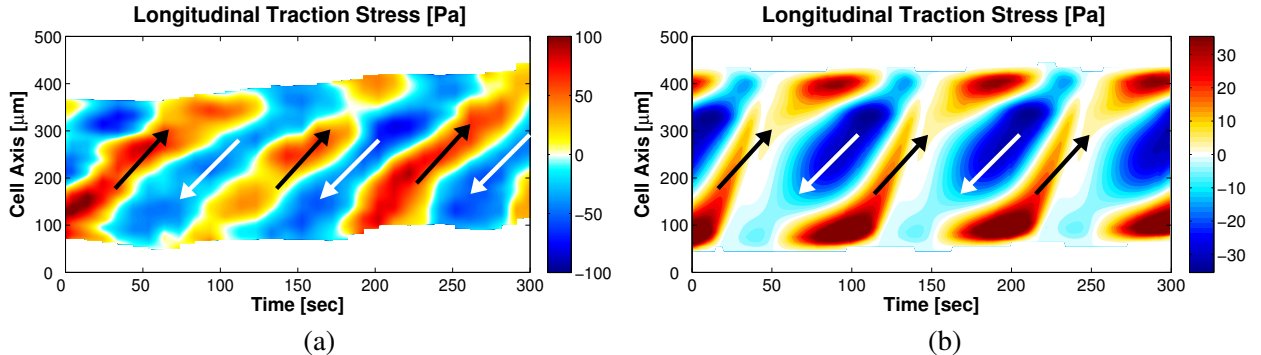


Figure 5: Kymographs of mean traction stress \bar{S} . (a) Data recorded in migrating physarum. (b) Values predicted by model simulation. Filled arrows indicate regions of stress directed forward. Open arrows indicate stress directed backward.

Figure 5(a) shows a kymograph of traction stresses measured in the same experiment as Figure 4(a) (with average cortical stresses removed). The data displayed are qualitatively represen-

tative of a large number of experiments. For comparison, Figure 5(b) shows a traction stress kymograph for the model cell. In the kymographs, we see a distinct phase wave of adhesion stress similar to the flow pattern in Figure 4. However, we note that in both experiments and our model, the phase velocity of the flow patterns is approximately four times faster than that of the traction stress patterns. The numerically calculated traction kymograph reproduces the main features of the traction stresses observed in live *physarum*. However, model and experiment do not agree in all respects. For example, for these parameters our model predicts the maximal forward stresses occur at the anterior and posterior of the cell while this does not appear to be the case in experiments. Altering parameters changes this aspect of the model predictions, but may cause other disagreements with experiments. It is difficult to identify by visual inspection which adhesion parameters *most closely* reproduce the spatiotemporal dynamics of the adhesion stress observed in experiments. In Section 4.5, we develop a more quantitative analysis of the coordination of adhesion to compare experiments and calculations.

4.3 Role of Flow

It is argued in [22] that the asymmetry in the motion of a fluid particle in such a flow pattern is directly responsible for the net displacement of the cell. Figure 6(a) illustrates this argument by showing particle paths in an idealized flow where regions of forward and backward flow propagate through the cell body. A particle translates forward and then backward with the same speed over one period of the wave. The particle is in a region of forward flow for more than half the period, resulting in net forward displacement. We define the asymmetry in the flow to be the ratio of the forward and backward displacement of such a particle path. Figure 6(b) shows the displacement of the centroid of a *physarum* specimen. We define the centroid displacement asymmetry to be the ratio of the forward and backward displacements of the centroid over one period. In Figure 6(c), we plot the asymmetry in the flow as a function of the centroid displacement asymmetry, measured in our experiments. If the flux of mass due to the intracellular flow wave were solely responsible for the migration of the cell center of mass, then the data in Figure 6(c) would lie on the green dashed line with slope 1. However, this line is in fact a poor fit to the data, while the best linear fit (solid blue line) has a much lower slope of ≈ 0.16 .

Examining Figure 6(c) more closely reveals a critical phenomenon. We observe that 45% of the data points have a flow asymmetry less than unity, despite having a centroid asymmetry greater than unity (lower right quadrant in the figure). Thus, for a significant fraction of our observations the intracellular flow suggests a net *backward* translation of mass, even though the cell has moved forwards. For comparison, in Figure 6(d), we show flow kymographs from two cells. Cell A (marked with upward triangles in Figure 6(c)) predominantly exhibits a flow asymmetry less than one, while Cell B (marked with downward triangles in Figure 6(c)) predominantly exhibits a flow asymmetry greater than one. Both exhibit similar phase velocities of the flow wave. While intracellular flow is likely to play a role in the migration of *physarum*, our experiments (and model predictions in Section 4.4) indicate that intracellular flow kinematics alone cannot determine the migration of the cell.

4.4 Adhesion Coordination and Crawling Speed

Figure 7 shows the centroid trajectories and flow kymographs for three cells generated with the model using different forms adhesion coordination. Cell A utilizes a phase parameter of $\phi = 3\pi/2$ and an adhesion coefficient of $A = 100\epsilon$. Cell C utilizes the same adhesion coefficient, and a reversed phase parameter of $\phi = \pi/2$. Cell B was simulated with $\phi = 3\pi/2$ and adhesion coefficient $A = 0$.

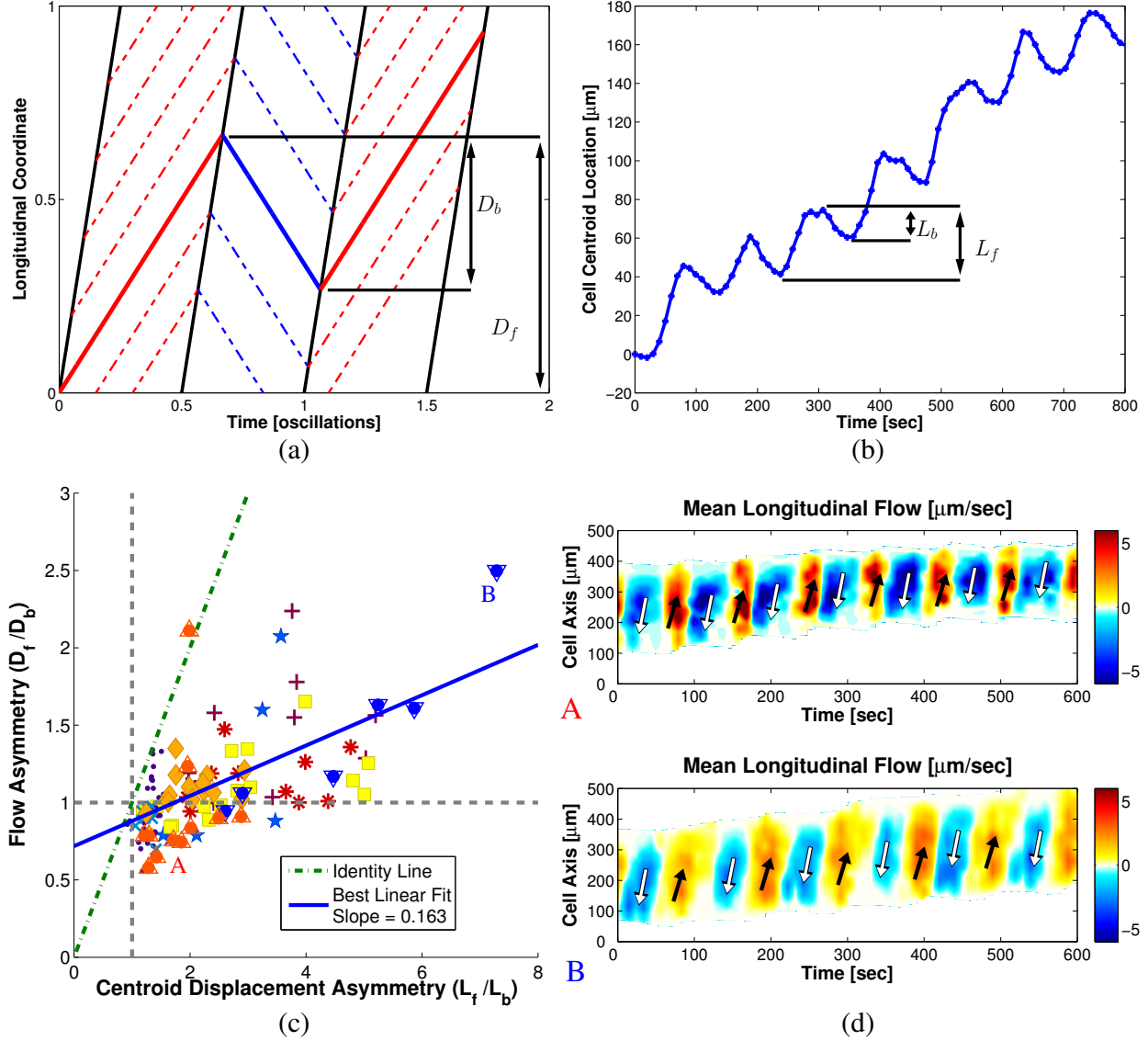


Figure 6: (a) An illustration of particle paths associated with a constant phase wave. The forward and backward particle displacements (D_f and D_b) are shown. Flow asymmetry is defined to be D_f/D_b . (b) A time series of the centroid of a migrating *physarum*. The forward and backward centroid displacements (L_f and L_b) are shown. Centroid displacement asymmetry is defined to be L_f/L_b . (c) Experimentally measured values of flow and centroid displacement asymmetry over 118 periods (each data point) and 9 cells (distinguished by distinct markers). The best linear fit is shown in blue. The line $D_f/D_b = L_f/L_b$ in green for comparison. (d) Flow kymographs from the cells marked A (upward triangles) and B (downward triangles) in (c), illustrating flow asymmetry less than and greater than one respectively.

All three of these cells are driven with the same contraction pattern, but more importantly exhibit very similar flow patterns which are all consistent with both our experiments and experiments of others [22, 43]. However, while cell A migrates forward consistent with experimental observations, cell B shows no net translation over the course of the simulation, and cell C migrates *backwards*. The implication is that while hydrodynamic effects may generate stresses integral to motility, it is

the coordination of the transmission of those stresses to the substrate that ultimately determines motility. Furthermore, from Cell B we see that *coordinated* adhesion is critical to motility. A cell migrating using just the nonspecific, uncoordinated adhesion (ϵ) fails to migrate.

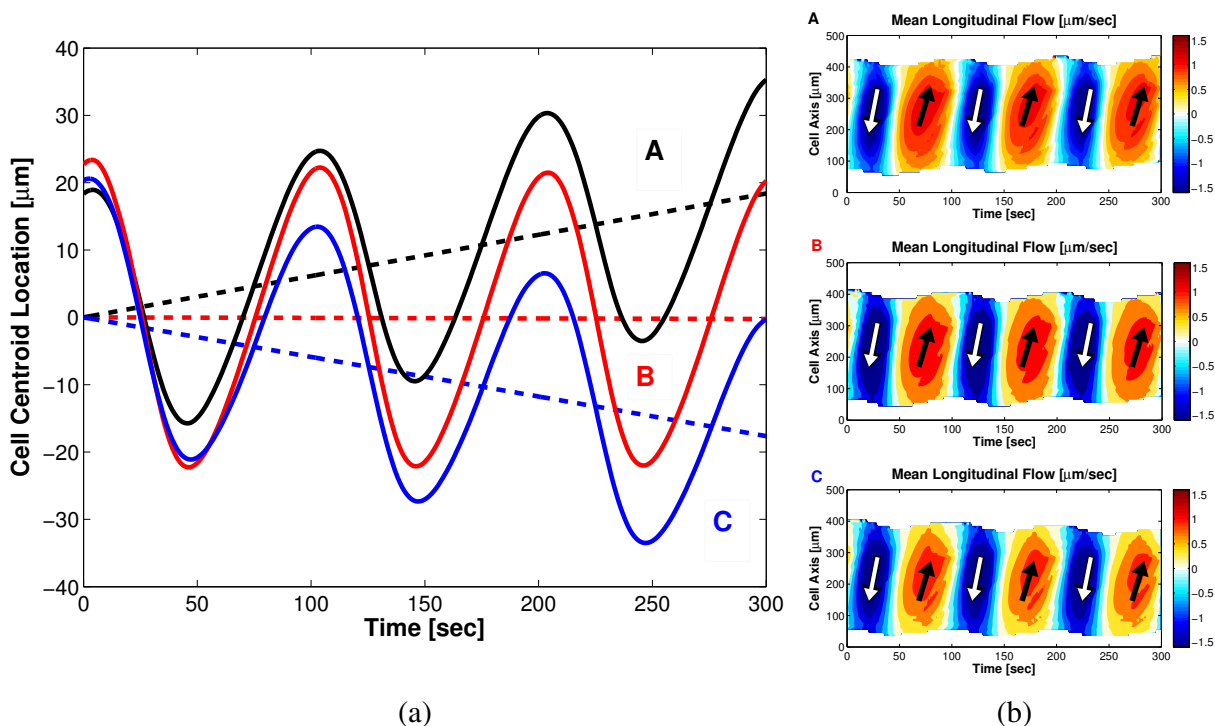


Figure 7: Numerically calculated time sequence of cell center is shown in (a). The solid lines indicate the centroids of individual cells, while the corresponding dashed lines indicates a best (least squares) linear fit. Migration speeds reported are given by the slope of this fit. The flow kymographs of \bar{U} for each cell are shown in (b). Filled arrows indicate forward flow. Open arrows indicate regions of backward flow.

For comparison, Figure 6(b) provides a time course of the center of a *physarum* specimen migrating in the lab. Qualitatively, the predicted migration behavior of model cell A closely matches that observed in our experiments. We see a distinct, periodic translation forward and backward, with a pronounced asymmetry to the two translations resulting in a net forward displacement of the cell. For the simulation shown, the net displacement of the model cell is approximately $6 \mu\text{m}$ per period, which is equivalent to an average migration velocity of $\approx 0.06 \mu\text{m}/\text{sec}$. In the laboratory, we measure *physarum* migrating at speeds of $0.169 \pm 0.041 \mu\text{m}/\text{sec}$ across the 10 cells which exhibit peristaltic behavior. Thus, our model predicts *physarum* migration in reasonable agreement with experiments, and suggests that coordination of adhesion and contraction is essential for efficient locomotion.

We now explore the speeds of migration predicted by the model as a function of adhesion strength and coordination. We perform simulations varying the phase parameter (ϕ) over eight equally spaced values from 0 to 2π , and the coefficient of adhesion (A) over 6 orders of magnitude. All parameter values give rise to similar periodic displacements (as shown in Figure 7). However, depending on the phase and strength of adhesion, our model predicts various translation velocities and *directions* of migration (Figure 8).

We observe that the migration velocity of the model cell is a non-monotonic function of adhesion

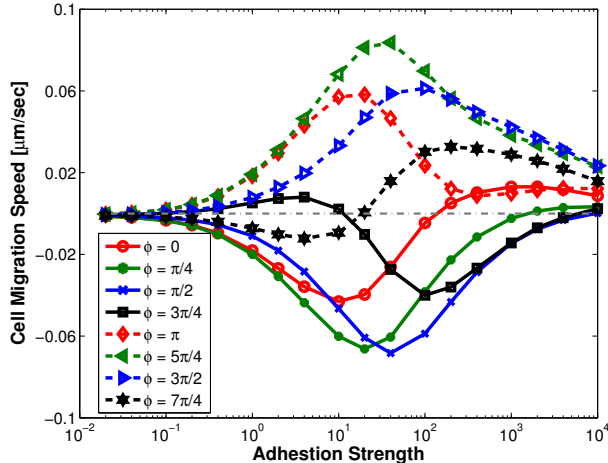


Figure 8: Average cell crawling speed as a function of adhesion coefficient and adhesion phase. Adhesion coefficient is reported in non-dimensional units $[A/\epsilon]$. Dashed grey line indicates zero migration velocity.

coordination and strength. Indeed, the cell speed is maximal at moderate values of coordinated adhesion, while uncoordinated or strongly adherent cells display negligible migration. In the limit $A \ll \epsilon$, the coordinated adhesion is negligible compared to the uniform, uncoordinated adhesion and the cell cannot move directionally despite generating periodic cell shape changes (see cell B in Figure 7). In the limit of strong adhesion $A \gg \epsilon$, the cell is effectively stuck to the substrate and cannot move even if this adhesion is highly coordinated. Experiments performed on highly adhesive substrates coated with collagen and the polycation poly-L-Lysine [31] are qualitatively consistent with the model predictions. *Physarum* amoebae migrating on these sticky substrates adopt a tadpole shape, and create peristaltic contraction waves and intracellular streaming. However, they barely move (see Supplementary Movie 4).

As each simulation is driven with active contractions of the same amplitude and form, we may consider migration speed of the cell as a measure of efficiency. The cell translates most efficiently with an active adhesion coefficient of $A/\epsilon \sim 10\text{--}100$, and a coordination phase of $\phi \sim \pi\text{--}3\pi/2$. Thus, the model predicts an optimal parameter regime in which to drive motility. However, the parameters A and ϕ are not measurable in our experiments. In the next section, we develop a quantitative measure of the relative timing of *flow* and *adhesion* within *physarum*. This will be used to determine if these model parameters are consistent with experiments.

4.5 Adhesion Correlation

We examine the time evolution of the strain energy exerted by live migrating *physarum* on their substrate (Equation S.5), and compare it with the evolution of the average intracellular flow velocity. The results show a distinct periodic pattern in both variables, with the flow wave preceding the adhesion wave by approximately a quarter period (Figure 9, left panel). This behavior is robust across the 9 reported experiments. To more precisely quantify this phase relationship between flow and adhesion energy, we calculate the cross correlation of flow and adhesion energy, as well as the autocorrelation of the flow wave (Figure 9, right panel). The distance between peaks of the autocorrelation function is interpreted as the period of the flow wave oscillation (T). The position of the first peak (restricted to times $t > 0$) of the cross correlation function indicates the relative

timing of the flow and energy waves (θ). The ratio θ/T defines the relative phase (between 0 and 1), which we measured to be 0.34 ± 0.07 in our experiments.

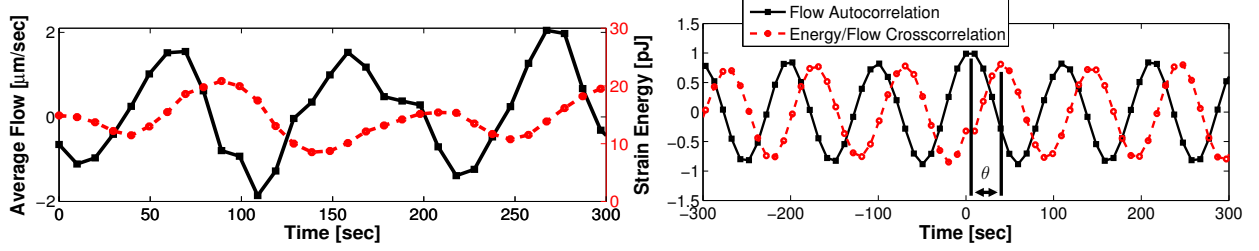


Figure 9: Experimentally measured flow (solid) and energy (dashed). Left panel shows average flow velocity within the cell interior, as well as total strain energy of adhesion as a function of time. Right panel shows auto and cross correlation of flow and energy, as well as the relative timing θ .

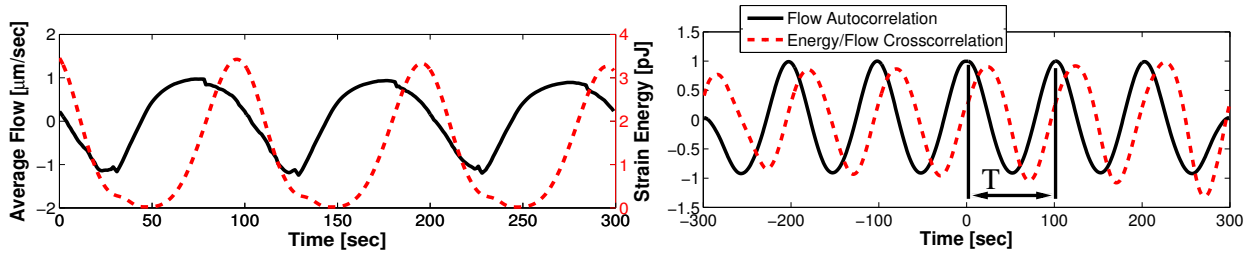


Figure 10: Numerically calculated flow (solid) and energy (dashed). Left panel shows average flow velocity within the cell interior, as well as total strain energy of adhesion as a function of time. Right panel shows auto and cross correlation of flow and energy, as well as the period T .

We perform the same analysis for the model simulations. Figure 10 shows the average intracellular fluid velocity and strain energy within the model adhesions, as well as the auto and cross correlation of these two time sequences. The data shown is for a cell with $\phi = 3\pi/2$ and $A = 100\epsilon$, which is the same parameter set used for the forward moving cell in Figure 7, as well as Figures 4 and 5. For these parameters, the model reproduces accurately the observed phase relationship between flow and energy waves. We see a clear phase lag of approximately a quarter period.

Given the good agreement between model and experiments, we utilize the phase relationship between flow and energy to identify plausible adhesion parameters in the model. The results are shown in Figure 11(a), where we report the relative phase lag of the energy wave, in periods of the wave, for all simulations shown in Figure 8. For reference, the relative phase observed in experiments (0.34 ± 0.07) is illustrated with the solid and dashed grey lines. The relative phase of adhesion energy appears to be highly sensitive to ϕ , and relatively insensitive to adhesion strength (beyond the range $A \approx \epsilon$). Values of ϕ in the range $3\pi/2 - 2\pi$ (2π and 0 are equivalent) produce a relative timing which is consistent with experimental measurements. Of these parameter values, $\phi = 3\pi/2$ is the only one which produces migration in the forward direction regardless of the strength of coordinated adhesion. For cells using $\phi = 3\pi/2$, the phase lag between flow and strain energy remains in the range 0.21–0.33 when varying the adhesion strength over 6 orders of magnitude. Specifically, in the case of highest migration velocity, we measure a phase lag of 0.25. In Figure 11(b) we show the average adhesion timing θ/T (calculated for all values $A > \epsilon$) and the maximum signed migration velocity for each value of the coordination parameter ϕ . Again, we see

that of the values of ϕ which are consistent with experiment, $\phi = 3\pi/2$ produces the maximum migration velocity.

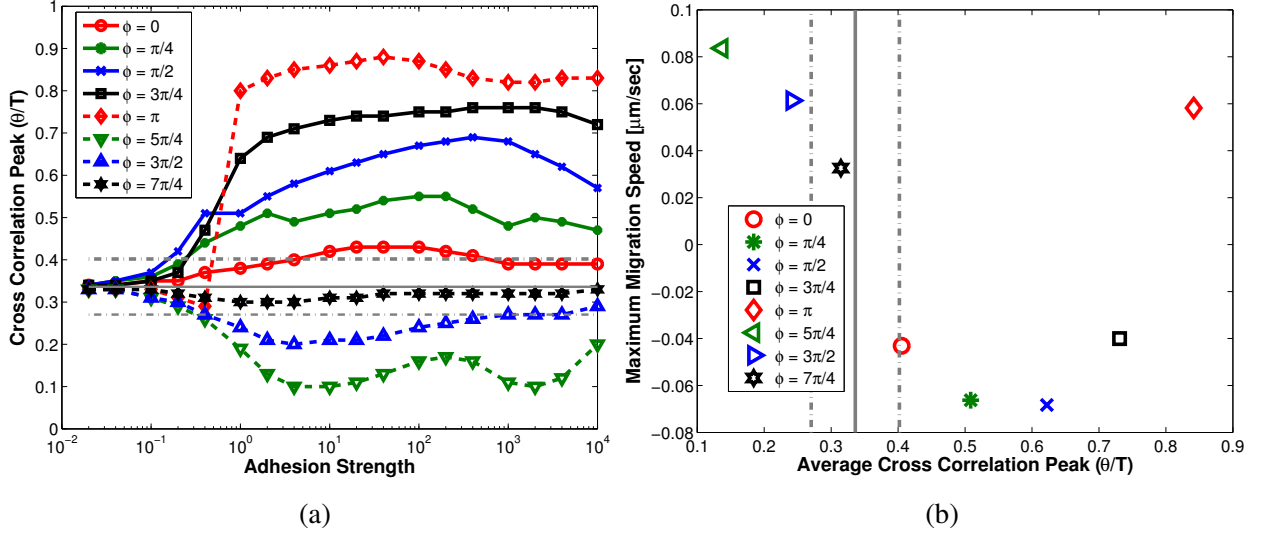


Figure 11: Panel (a) shows maximum cross correlation of elastic energy of adhesion and average cytoplasmic flow. Adhesion coefficient is reported in non dimensional units $[A/\epsilon]$. Horizontal grey lines indicates experimentally measured phase of 0.34 ± 0.07 . Panel (b) shows the average adhesion timing and maximum migration speed for each value of adhesion coordination ϕ . Vertical grey lines indicates experimentally measured phase of 0.34 ± 0.07

4.6 Robustness

From the criteria discussed above, the spatiotemporal pattern of adhesion which is most consistent with experimental evidence corresponds to a phase lag of $\phi \approx 3\pi/2$ and a strength of $A \approx 100\epsilon$. Furthermore, these parameters predict nearly optimal migration velocity within the constraints of the model. It is noteworthy that this optimal migration velocity is not sensitive to the strength of adhesion. Returning to Figure 8, we see that the model predicts a migration velocity above $0.03 \mu\text{m}/\text{sec}$ (roughly 50% of maximal) over more than *two decades* of adhesion strength. Thus far, our simulations consider only spatially uniform substrates. In relevant environments, the strength of adhesive interactions between the cell and substrate is not homogenous, as numerous extracellular and intracellular factors may affect such interactions. Therefore, we modify our model to quantify the robustness of migration with respect to spatial variations in adhesion strength. We alter the model of cell adhesions to the substrate in order to incorporate spatial heterogeneity. The existing form of adhesion (eq. (7)) is replaced with

$$\zeta(x, t) = \frac{A}{2} g(x_{\text{lab}}, y_{\text{lab}}) \left(\cos \left(\frac{2\pi}{\ell_{\text{adh}}} x - \frac{2\pi}{T} t + \phi \right) + 1 \right) + \epsilon, \quad (10)$$

where $g(x_{\text{lab}}, y_{\text{lab}})$ is a randomly constructed function of fixed laboratory coordinates. By construction, this function has mean of $\mu_r = 1$ and standard deviation $\sigma_r = 0.34$ (for further details, see Supplemental Information). This has the effect of spatially modulating the strength with which the cell adheres to the substrate.

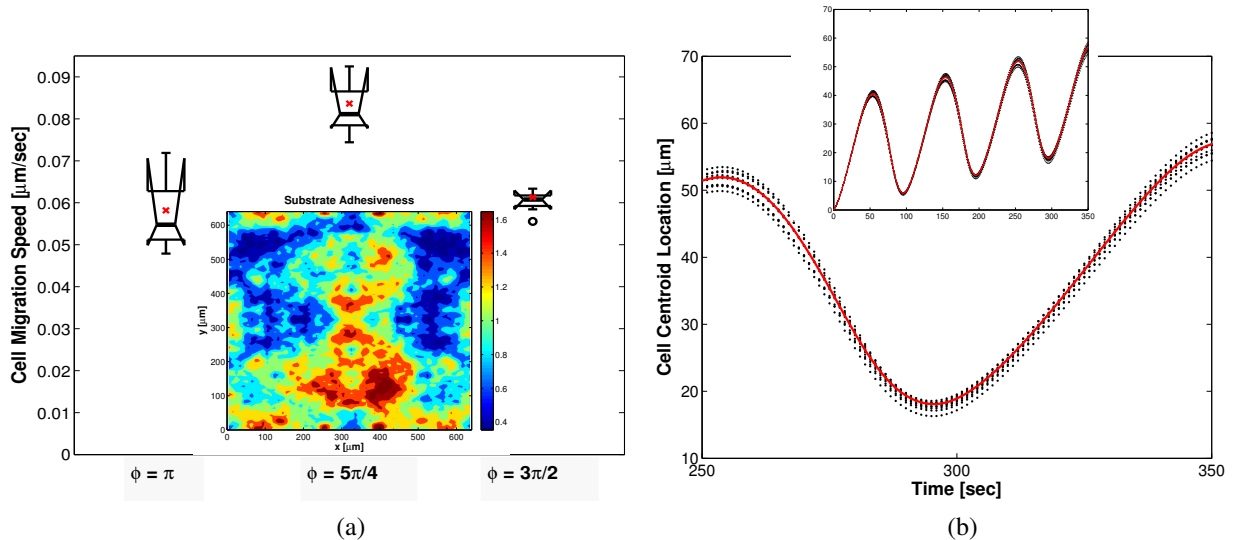


Figure 12: (a) Open circles indicate outliers in data set. Filled red points indicate the migration velocity calculated for a cell migrating across a homogeneous substrate. The inset shows a single randomly generated example of the spatial heterogeneity $g(x, y)$. (b) Dashed black lines indicate time course of centroids of cells migrating across random substrate. Solid red line indicates cell migrating across homogeneous substrate. $\phi = 3\pi/2$ in all cases.

Using the randomly constructed function g to represent a heterogeneous substrate, we simulated cells migrating across ten different substrates. We performed these simulations for the three values of ϕ which generically resulted in forward migration, and values of coordinated adhesion that results in the greatest migration velocity for each phase parameter. This means $\phi = \pi$, $5\pi/4$, and $3\pi/2$, with $A = 20\epsilon$, 40ϵ , and 100ϵ , respectively. The results are summarized in the box plot of Figure 12(a). The spread of the data shows that migration speed is relatively insensitive to substrate heterogeneity for the considered values of ϕ . Notice that the value $\phi = 3\pi/2$, which is most consistent with our live *physarum* experiments, produces a substantially lower spread in migration speed, with half the data falling within $\pm 2.5\%$ of the median value. Thus, this spatiotemporal pattern of adhesion coordination is highly robust with respect to local variations in the strength of substrate adhesiveness.

Figure 12(b) shows the time evolution of the centroid of the 10 cells with random adhesion strength for $\phi = 3\pi/2$ (black), compared with the homogeneous substrate case (red). The inset shows the full time course, while the main panel shows just the final 100 sec of migration. Over time, the location of the cells migrating across random substrates begins to deviate as random effects accumulate over time. However, these deviations are quite small compared to the scale of cell migration. This result indicates that, for the set of model parameters that reproduce the experimental measurements, the instantaneous speed of migration is remarkably insensitive to the spatial heterogeneity of the substrate throughout the whole oscillation period.

5 Discussion

Migrating amoeboid cells such as *physarum* microplasmidia apply highly dynamic traction forces on their surroundings, leading to large shape changes and fast intracellular streaming flows. However,

there is a paucity of simultaneous measurements of traction forces and intracellular streaming, which has made it difficult to develop mechanistic models that relate the forces driving amoeboid motion and the cellular deformations realizing this motion.

In this work, we combine simultaneous measurements of cytoplasmic flow and the traction stresses in migrating *physarum* microplasmodia, with detailed computational models of amoeboid migration that resolve the mechanics of cellular deformation and substrate adhesion. Our measurements reveal that *physarum* amoebae move by creating traveling waves of contractile traction stresses with a well defined period of ~ 100 sec. The traction stress waves are similar in character to the previously observed waves of intracellular flow, but the flow waves consistently precede the stress waves by $\sim 1/4$ cycle. Inspired by this observation, we use our numerical model to investigate the consequences of migration using traveling waves of coordinated contraction and adhesion. Our investigations show that, by altering the timing of adhesion relative to the flow wave, the cell is able to migrate with different velocities and in different directions. These findings transform the previously established view that directional migration of *physarum* amoebae is caused by the directionality of the flow waves [22].

By juxtaposing our modeling and experimental work, we have identified specific forms of generation and transmission of cellular forces which plausibly drive the migration of *physarum* amoebae. Within the context of our adhesion model, our simulations and experiments reveal a distinct pattern of spatiotemporal coordination between contraction and adhesion which reproduces the experimentally measured cytoplasmic flows and traction stresses, and the scale of cell migration speed. This coordination pattern consists of a phase lag of $3/4$ cycle between adhesion and contraction ($\phi \approx 3\pi/2$). In addition to validating the model, this result provides insight into the underlying mechanism of amoeboid motility. The particular adhesion coordination pattern we highlight is extremely robust to perturbations in adhesive interactions with the extracellular environment, and results in nearly maximum migration speed within the context of the model. Interestingly, the adhesion coordination pattern that produces maximum migration speed ($\phi = 5\pi/4$) is less robust, possibly because it does not properly reproduce the relative timing of flow and traction stress. This insight into the potential compromises of different adhesion coordination would not have been possible through experimental investigations alone. Our model allows us a direct control over the coordination of adhesion that we are unable to control in a laboratory setting.

We note that our frictional adhesion model is rather independent of the precise nature of the cell-substrate interactions. While this model could be justified as a time averaged effect of integrin-like molecular binding, this assumption is not necessary to arrive at the precise mathematical form that we use. Indeed, it is unclear how *physarum* exerts stresses on its surroundings. Previous models have suggested that wave-like patterns of contraction may spontaneously arise from the coupling of the mechanics and chemistry of contraction in *physarum* [21, 20]. It is plausible that a similar mechanism may give rise to a wave-like modulation of the strength of adhesive interactions. Though it is unlikely that microplasmodia migrate utilizing adhesive patterns as simple as our idealized wave of adhesion, our modeling assumptions are consistent with a variety of possible mechanisms. More experimental investigation into the specific nature of *physarum*-substrate interaction is required.

While somewhat unique, the motility of *physarum* microplasmodia shares fundamental characteristics with other forms of amoeboid migration. Rhythmic cellular contractions of period ~ 100 sec are known to drive the motion of neutrophil-like and *Dictyostelium* amoeboid cells [42, 7]. In particular, while intracellular flow kinematics do not fully determine the motility of *physarum*, our results suggest that cellular contractions are used to generate intracellular flows and cell locomotion. The use of pressure-driven flows of cytoplasm to generate translation has been widely observed in motile cells [39, 14, 7]. This is in contrast to cell types which utilize the polarity of actin filaments to generate polymerization-driven protrusions such as lamellapodia and filapodia

[2]. Our experimental model does not generalize to this type of motility, but our modeling framework could be adapted to account for network polarity and polymerization stresses. Furthermore, the observed motility of *physarum* is consistent with a model of cell-ECM interaction that does not require specific integrin-like binding molecules. It has been shown that neutrophils undergo amoeboid migration in three dimensional environments in the absence of specific binding molecules [17]. This contributes to the growing notion that friction mediated motility is biologically advantageous, as it is robust to geometric and mechanical changes in the ECM [35, 14].

The form of amoeboid motility we observe in *physarum* also shares many characteristics with locomotion in higher organisms. The traveling wave of contraction is similar to contraction patterns observed in migrating gastropods, annelids, and *dictyostelium* slugs. In both experimental and theoretical investigations of these organisms, it has been seen that the direction of contraction wave propagation is not the critical factor in determining migration direction. Rather, migration results from the timing of interactions between the organism and substrate [29, 6]. As we have previously discussed, this same behavior is observed in our model.

While *physarum* locomotion shares this behavior with various gastropods and annelids, we note that the amoeba moves on a vastly different scale than these organisms. The slugs observed in [29] ranged from 0.7-28 cm in length, while *physarum* microplasmodia begin to migrate in this fashion after reaching a size of approximately 100 μm . This seems to indicate that a motility mechanism predicated on traveling waves of strain and appropriately timed adhesive interactions represents a robust design principle; one which is viable across length scales from cellular to macro. Indeed, the advantageous characteristics of *physarum* have not gone unnoticed by the robotics community, where the organism has been the inspiration for biomimetic design [36, 40].

Acknowledgements We would like to thank T. Nakagaki and J.P. Rieu for their stimulating discussions, which contributed to this work. We would also like to acknowledge the input of Ruedi Meili and Juan C. Lasheras. Authors Lewis and Guy were supported by NSF grant DMS-1160438 and NSF grant DMS-1226386. Authors Zhang and del Álamo were supported by NSF grant CBET-1055697 and National Institutes of Health grant 5R01GM084227-03.

References

- [1] Tinevez, J.-Y., Schulze, U., Salbreux, G., Roensch, J., Joanny, J. F. & Paluch, E. 2009 Role of Cortical Tension in Bleb Growth. *Proceedings of the National Academy of Sciences*, **106**, 18581–18586.
- [2] Blanchoin, L., Boujemaa-Paterski, R., Sykes, C. & Plastino, J. 2014 Actin Dynamics, Architecture, and Mechanics in Cell Motility. *Physiological Reviews*, **94**, 235–263.
- [3] Alvarez-Gonzalez, B., Meili, R., Bastounis, E., Firtel, R. A., Lasheras, J. C. & Del Alamo, J. C. 2015 Three-Dimensional Balance of Cortical Tension and Axial Contractility Enables Fast Amoeboid Migration. *Biophysical Journal*, **108**, 821–832.
- [4] Lewis, O., Zhang, S., Guy, R. D. & Del Álamo, J. C. 2014. Traction Force Microscopy and Particle Image Velocimetry of Migrating Physarum. <http://dx.doi.org/10.6084/m9.figshare.1267558>.
- [5] Lewis, O. L. 2014 Mathematical Investigation of Hydrodynamic Contributions to Amoeboid Cell Motility in Physarum polycephalum. Ph.D. thesis, University of California Davis.
- [6] Tanaka, Y., Ito, K., Nakagaki, T. & Kobayashi, R. 2012 Mechanics of Peristaltic locomotion and Role of Anchoring. *Journal of the Royal Society Interface*, **9**, 222–233.
- [7] Bastounis, E., Meili, R., Alvarez-Gonzalez, B., Francois, J., Del Alamo, J. C., Firtel, R. A. & Lasheras, J. C. 2014 Both Contractile Axial and Lateral Traction Force Dynamics Drive Amoeboid Cell Motility. *Journal of Cell Biology*, **204**, 1045–1061.
- [8] Stockem, W. & Brix, K. 1994 Analysis of Microfilament Organization and Contractile Activities in Physarum. *International Review of Cytology - A Survey of Cell Biology*, **149**, 145–215.
- [9] Norris, C. H. 1940 Elasticity Studies on the Myxomycete, Physarum Polycephalum. *Journal of Cellular and Comparative Physiology*, **16**, 313–322.
- [10] Tse, J. R. & Engler, A. J. 2010 Preparation of Hydrogel Substrates with Tunable Mechanical Properties. *Current protocols in Cell Biology*, **Chapter 10**, 10.16.1–10.16.16.
- [11] Moeendarbary, E., Valon, L., Fritzsche, M., Harris, A. R., Moulding, D. A., Thrasher, A. J., Stride, E., Mahadevan, L. & Charras, G. T. 2013 The Cytoplasm of Living Cells Behaves as a Poroelastic Material. *Nature Materials*, **12**, 253–261.
- [12] Mittal, R. & Iaccarino, G. 2005 Immersed Boundary Methods. *Annual Review of Fluid Mechanics*, **37**, 239–261.
- [13] Ohl, C. & Stockem, W. 1995 Distribution and Function of Myosin II as a Main Constituent of the Microfilament System in Physarum Polycephalum. *European Journal of Protistology*, **31**, 208–222.
- [14] Tozluoğlu, M., Tournier, A. L., Jenkins, R. P., Hooper, S., Bates, P. A. & Sahai, E. 2013 Matrix Geometry Determines Optimal Cancer Cell Migration Strategy and Modulates Response to Interventions. *Nature Cell Biology*, **15**, 751–762.
- [15] Peskin, C. S. 1977 Numerical Analysis of Blood Flow in the Heart. *Journal of Computational Physics*, **25**, 220–252.

- [16] Brix, K. & Stockem, W. 1987 Studies on Microplasmidia of *Physarum polycephalum*. *Cell Biology International Reports*, **11**, 529–536.
- [17] Lämmermann, T., Bader, B. L., Monkley, S. J., Worbs, T., Wedlich-Söldner, R., Hirsch, K., Keller, M., Förster, R., Critchley, D. R. *et al.* 2008 Rapid Leukocyte Migration by Integrin-Independent Flowing and Squeezing. *Nature*, **453**, 51–55.
- [18] Keren, K., Yam, P. T., Kinkhabwala, A., Mogilner, A. & Theriot, J. A. 2009 Intracellular Fluid Flow in Rapidly Moving Cells. *Nature Cell Biology*, **11**, 1219–1224.
- [19] Bausch, A. R., Ziemann, F., Boulbitch, A. A., Jacobson, K. & Sackmann, E. 1998 Local Measurements of Viscoelastic Parameters of Adherent Cell Surfaces by Magnetic Bead Microrheometry. *Biophysical Journal*, **75**, 2038–2049.
- [20] Radszweit, M., Engel, H. & Bär, M. 2014 An Active Poroelastic Model for Mechanochemical Patterns in Protoplasmic Droplets of *Physarum polycephalum*. *PLoS ONE*, **9**, e99220.
- [21] Radszweit, M., Alonso, S., Engel, H. & Bär, M. 2013 Intracellular Mechanochemical Waves in an Active Poroelastic Model. *Physical Review Letters*, **110**, 138102.
- [22] Matsumoto, K., Takagi, S. & Nakagaki, T. 2008 Locomotive Mechanism of *Physarum Plasmodia* Based on Spatiotemporal Analysis of Protoplasmic Streaming. *Biophysical Journal*, **94**, 2492–2504.
- [23] Srinivasan, M. & Walcott, S. 2009 Binding Site Models of Friction Due to the Formation and Rupture of Bonds: State-Function Formalism, Force-Velocity Relations, Response to Slip Velocity Transients, and Slip Stability. *Physical Review E*, **80**, 046124.
- [24] Rieu, J.-P., Barentin, C., Maeda, Y. & Sawada, Y. 2005 Direct Mechanical Force Measurements During the Migration of *Dictyostelium* Slugs Using Flexible Substrata. *Biophysical Journal*, **89**, 3563–3576.
- [25] Yamada, S., Wirtz, D. & Kuo, S. C. 2000 Mechanics of Living Cells Measured by Laser Tracking Microrheology. *Biophysical Journal*, **78**, 1736–1747.
- [26] Hayase, M., Maekawa, A., Yubisui, T. & Minami, Y. 2008 Properties, Intracellular Localization, and Stage-Specific Expression of Membrane-Bound Beta-Glucosidase, BglM1, From *Physarum Polycephalum*. *The International Journal of Biochemistry & Cell Biology*, **40**, 2141–2150.
- [27] Engler, A., Bacakova, L., Newman, C., Hategan, A., Griffin, M. & Discher, D. 2004 Substrate Compliance Versus Ligand Density in Cell on Gel Responses. *Biophysical Journal*, **86**, 617–628.
- [28] Charras, G. T., Mitchison, T. J. & Mahadevan, L. 2009 Animal Cell Hydraulics. *Journal of Cell Science*, **122**, 3233–3241.
- [29] Lai, J. H., Alamo, J. C., Rodríguez-Rodríguez, J. & Lasheras, J. C. 2010 The Mechanics of the Adhesive Locomotion of Terrestrial Gastropods. *Journal of Experimental Biology*, **213**, 3920–3933.
- [30] Allen, R. D., Pitts, W. R., Speir, D. & Brault, J. 1963 Shuttle-Streaming: Synchronization with Heat Production in Slime Mold. *Science*, **142**, 1485–1487.

- [31] Jay, P. Y., Pham, P. A., Wong, S. A. & Elson, E. L. 1995 A Mechanical Function of Myosin II in Cell Motility. *Journal of Cell Science*, **108** (Pt 1), 387–393.
- [32] Del Alamo, J. C., Meili, R., Alvarez-Gonzalez, B., Alonso-Latorre, B., Bastounis, E., Firtel, R. & Lasheras, J. C. 2013 Three-Dimensional Quantification of Cellular Traction Forces and Mechanosensing of Thin Substrata by Fourier Traction Force Microscopy. *PLoS ONE*, **8**, e69850.
- [33] Butler, J. P., Tolic-Norrelykke, I. M., Fabry, B. & Fredberg, J. J. 2002 Traction Fields, Moments, and Strain Energy That Cells Exert on Their Surroundings. *American Journal of Physiology - Cell Physiology*, **282**, C595–C605.
- [34] Strychalski, W., Copos, C. A., Lewis, O. L. & Guy, R. D. 2015 A Poroelastic Immersed Boundary Method with Applications to Cell Biology. *Journal of Computational Physics*, **282**, 77 – 97.
- [35] Charras, G. & Paluch, E. 2008 Blebs Lead the Way: How to Migrate Without Lamellipodia. *Nature Reviews: Molecular Cell Biology*, **9**, 730–736.
- [36] Piovaneli, M., Fujie, T., Mazzolai, B. & Beccai, L. 2012 A Bio-Inspired Approach Towards the Development of Soft Amoeboid Microrobots. In *Biomedical Robotics and Biomechanics, the IEEE RAS EMBS International Conference on*, pp. 612–616. IEEE.
- [37] Wang, Y. L. & Pelham, R. J. 1998 Preparation of a Flexible, Porous Polyacrylamide Substrate for Mechanical Studies of Cultured Cells. *Methods in Enzymology*, **298**, 489–496.
- [38] Charras, G. T., Yarrow, J. C., Horton, M. A., Mahadevan, L. & Mitchison, T. J. 2005 Non-Equilibration of Hydrostatic Pressure in Blebbing Cells. *Nature*, **435**, 365–369.
- [39] Lämmermann, T. & Sixt, M. 2009 Mechanical Modes of ‘Amoeboid’ Cell Migration. *Current Opinion in Cell Biology*, **21**, 636–644.
- [40] Umedachi, T., Idei, R., Ito, K. & Ishiguro, A. 2013 True-Slime-Mould-Inspired Hydrostatically Coupled Oscillator System Exhibiting Versatile Behaviours. *Bioinspiration & Biomimetics*, **8**, 035001.
- [41] Kukulies, J., Brix, K. & Stockem, W. 1987 Studies on Microplasmodia of *Physarum polycephalum*. *Cell and Tissue Research*, **250**, 125–134.
- [42] Del Alamo, J. C., Meili, R., Alonso-Latorre, B., Rodriguez-Rodriguez, J., Aliseda, A., Firtel, R. A. & Lasheras, J. C. 2007 Spatio-Temporal Analysis of Eukaryotic Cell Motility by Improved Force Cytometry. *Proceedings of the National Academy of Sciences*, **104**, 13343–13348.
- [43] Koya, S. & Ueda, T. 1998 The Onset of Rhythmic Streaming in the *Physarum* Plasmodium. *ACH, models in chemistry*, **135**, 297–304.
- [44] Willert, C. E. & Gharib, M. 1991 Digital Particle Image Velocimetry. *Experiments in Fluids*, **10**, 181–193.
- [45] Dembo, M. & Wang, Y. L. 1999 Stresses at the Cell-to-Substrate Interface During Locomotion of Fibroblasts. *Biophysical Journal*, **76**, 2307–2316.
- [46] Bray, D. 2001 *Cell Movements. From Molecules to Motility*. New York: Garland.

- [47] Edelstein, A., Amodaj, N., Hoover, K., Vale, R. & Stuurman, N. 2010 Computer Control of Microscopes Using μ Manager. *Current Protocols in Molecular Biology*, **Chapter 14**, 14.20.1–14.20.17.
- [48] Peskin, C. S. 2002 The Immersed Boundary Method. *Acta Numerica*, **11**, 479–517.
- [49] Wang, N., Butler, J. P. & Ingber, D. E. 1993 Mechanotransduction Across the Cell Surface and Through the Cytoskeleton. *Science*, **260**, 1124–1127.
- [50] Strychalski, W. & Guy, R. D. 2013 A Computational Model of Bleb Formation. *Mathematical Medicine and Biology : A Journal of the IMA*, **30**, 115–130.
- [51] Rieu, J.-P., Delanöe-Ayari, H., Takagi, S., Tanaka, Y. & Nakagaki, T. Periodic Traction in Migrating Large Amoeba of *Physarum polycephalum*. *Submitted*.
- [52] Álvarez-González, B., Meili, R., Bastounis, E., Titus, M., Firtel, R. A., Lasheras, J. C. & del Álamo, J. C. 2015. 3-D Balance of Cortical Tension and Axial Contractility Enables Fast Amoeboid Migration, Submitted.

Coordination of Contractility, Adhesion and Flow in Migrating *Physarum* Amoebae

Owen L. Lewis, Shun Zhang, Robert D. Guy & Juan C. del Álamo

March 30, 2015

S Supplemental Information

S.1 Experimental Materials and Methods

Cell preparation *Physarum* Plasmodia were grown from sporae on 1% agar gel (Granulated; BD) using $150 \times 15\text{mm}$ culture plates (BD), fed with oat flakes (QUAKER) and kept in a dark humid environment at room temperature. Small portions of $\sim 1 \times 1 \text{ mm}^2$ were cut from the plasmodium tips, transferred to a new agar plate and kept overnight until they developed a tubular shape. The process was repeated to harvest a smaller portion of $\sim 0.2 \times 0.2 \text{ mm}^2$, resulting in a single migrating amoeba with noticeable intracellular streaming.

Substrate fabrication Collagen-coated Polyacrylamide PA gels were prepared for traction force microscopy as previously described [1], following well-established protocols [2, 3]. The gel was ~ 1.5 mm thick and consisted of two layers; the bottom one contained no florescent beads, while the top one was thin ($\sim 10\mu\text{m}$) and contained $0.5\mu\text{m}$ florescent beads (FluoSperes; Molecular Probes). The gels were fabricated using 5% acrylamide and 0.3% bisacrylamide (Fisher BioReagents), resulting in values of the Poisson ratio and Young's modulus equal to 0.46 and 8.73 kPa respectively [4]. Single amoebae were transferred from the agar culture plates and seeded on top of the polyacrylamide gel. A 3 mm-thick cap made of 0.8 % agarose was placed over the amoebae immediately after. The weight of the agar cap generated a pressure on the amoebae (≈ 30 Pa) which is comparable to but smaller than the traction stresses generated by the cells, thus generating a gentle confinement. Such confinement prevented the PA gel from drying out and rendered the intracellular flows easier to visualize, while at the same time allowing the cell to generate measureable deformations in its surroundings. A simple schematic of the gel-agar cap apparatus can be found in Figure S.1.

Microscopy A Leica DMI 6000B inverted microscope and a PC running Micro-Manager software were used for image acquisition [5]. Time-lapse sequences were obtained at 16X by alternating bright-field and fluorescence acquisitions every 12 sec. First, 10 images were acquired in the bright field for intracellular flow quantification at a frame rate of 5 Hz. Then, a 40-image fluorescence z-stack ($\Delta z = 1\mu\text{m}$) was acquired for traction force microscopy over 10 sec. This alternating sequence was repeated until the cell moved out of the field of view, allowing us to obtain a quasi-simultaneous quantification of intracellular streaming and traction stresses during *physarum* migration, given that the timescale of this phenomenon is ~ 100 sec [6]. Additionally, we performed a number of experiments where we continuously acquired bright field images at 5 Hz to quantify intracellular

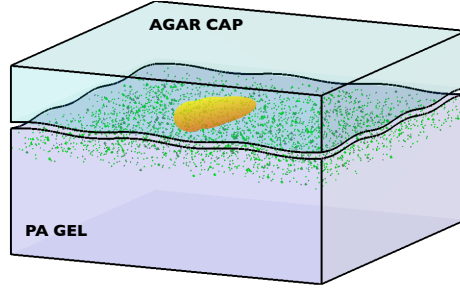


Figure S.1: Schematic of a *physarum* specimen between an agar cap and Polyacrylamide gell substrate.

streaming at high time resolution. An image set from an example cell (both bright field and florescence z-stacks) is available online at [7].

Flow Quantification The cytoplasm of *physarum* amoebae is densely packed with vesicles that can be used as flow tracers to quantify the intracellular streaming velocity by particle image velocimetry (PIV) [6, 8]. A common feature of shuttle streaming in *physarum* is the occurrence of narrow ($\sim 20\mu\text{m}$ in diameter) channels, inside of which the flow speed is much higher than outside. To accurately resolve these channels, we pre-process the raw image sequences using high-pass, band-pass and low-pass temporal filters,

$$I_{High}(t) = \frac{1}{6}I(t-2) - \frac{4}{6}I(t-1) + I(t) - \frac{4}{6}I(t+1) + \frac{1}{6}I(t+2), \quad (\text{S.1})$$

$$I_{Band}(t) = -\frac{1}{2}I(t-2) + I(t) - \frac{1}{2}I(t+2), \quad (\text{S.2})$$

$$I_{Low}(t) = \frac{1}{4}I(t-1) + \frac{1}{2}I(t) + \frac{1}{4}I(t+1), \quad (\text{S.3})$$

where I denotes the raw images and t is the acquisition time point. Then, we ran our in-house PIV algorithm on each one of the filtered image sequences I_{high} , I_{band} and I_{low} . At each point in space and time, we assigned the velocity vector resulting from the filtered sequence that maximizes the PIV signal-to-noise ratio. The PIV interrogation window size and spacing were respectively 32 and 8 pixels, yielding a spatial resolution of $6.5 \mu\text{m}$.

Measurement of substrate deformation and determination of traction stresses The three-dimensional deformation of the polyacrylamide substrate was measured at its top surface on which the *physarum* amoebae were migrating, as described by del Álamo et al. [1]. Each instantaneous fluorescence z-stack marking the positions of the beads in the gel was cross-correlated with a reference z-stack in which the substrate was not deformed; the latter was typically obtained by waiting until the cell moved out of the field of view. The comparison between the deformed and undeformed (reference) images was carried out by dividing each instantaneous and reference z-stack into interrogation boxes and optimizing the cross-correlation between each pair of interrogation

boxes in three-dimensions, similar to PIV. We used interrogation boxes of $32 \times 32 \times 40$ pixels with a 50% overlap in x and y directions, leading to a spatial resolution of $13 \mu m$.

Using these measurements as boundary conditions, we computed the three-dimensional deformation field in the whole polyacrylamide substrate by solving the elasticity equation of equilibrium for a linear, homogeneous, isotropic three-dimensional body,

$$(1 - 2\sigma)\nabla\vec{c} + \nabla(\nabla \cdot \vec{c}) = 0, \quad (\text{S.4})$$

where \vec{c} is the deformation field and σ is the poisson ratio. The exact analytical solution to this problem can be found elsewhere [9, 1].

The traction stress $\vec{\tau} = (\tau_{xz}, \tau_{yz}, \tau_{zz})$ exerted by the cell on the substrate is then obtained from the computed deformation field. The mechanical work exerted by the cell on the substrate, which is also the strain energy stored in the deformed gel is

$$E_{elas} = \frac{1}{2} \int_S \vec{\tau}(z = h) \cdot \vec{c}(z = h) dS \quad (\text{S.5})$$

Removing Average Cortical Stress For each time point we calculate the “moving average” stress field

$$\vec{\tau}_{\text{avg}}(t) = \frac{1}{t_2 - t_1} \int_{t_1}^{t_2} \vec{\tau}(t') dt'. \quad (\text{S.6})$$

Here, $\vec{\tau}(t)$ is the instantaneous traction stress field and t_1 and t_2 are the time points represent the beginning of the previous cycle and the end of the following cycle (measured with respect to t). We then calculate the dynamic instantaneous stress, defined as

$$\vec{\tau}_{\text{dyn}} = \vec{\tau}(t) - \vec{\tau}_{\text{avg}}. \quad (\text{S.7})$$

The field $\vec{\tau}_{\text{dyn}}$ is the quantity which we report in most of the body of this work.

S.2 Computational Model Details

S.2.1 Mixed Eulerian-Lagrangian Model

Our mathematical model is based on the Immersed Boundary (IB) method, which was originally developed to simulate blood flow [10], but has since been adopted to address an array of fluid-structure interaction problems in biology and engineering [11]. The key feature of the IB method is that the equations of fluid mechanics are solved in a fixed Eulerian coordinate system (with coordinate \vec{x}_{lab} and domain Ω), while the equations of the immersed solid structure are represented in a moving Lagrangian coordinate system (with coordinate \vec{x} and domain Γ). In the context of the present work, the Eulerian fluid represents the viscous cytosol which permeates the cell interior, while various Lagrangian structures will represent the various intracellular structures. Transforms between the two coordinate systems are accomplished by the so called spread and interpolation operators, which are both convolutions against a delta distribution kernel [12]. The spreading operator, denoted by \mathcal{S} , maps Lagrangian quantities to the Eulerian coordinate system via

$$\vec{v} = \mathcal{S}\vec{V} = \int_{\Gamma} \vec{V} \delta(\vec{X}(\vec{x}, t) - \vec{x}_{\text{lab}}) d\vec{x}. \quad (\text{S.8})$$

Similarly, the interpolation operator, denoted by \mathcal{S}^* , maps from Eulerian coordinates to Lagrangian,

$$\vec{V} = \mathcal{S}^*\vec{v} = \int_{\Omega} \vec{v} \delta(\vec{X}(\vec{x}, t) - \vec{x}_{\text{lab}}) d\vec{x}_{\text{lab}}. \quad (\text{S.9})$$

We use the convention that quantities defined as a function of the Eulerian coordinate are denoted with lower case letters, while functions of Lagrangian coordinate are denoted with upper case letters. For example, the instantaneous location of a material point of the cytoskeleton is given by $\vec{X}(\vec{x}, t)$. Recall that the force balance equations which describe our model are

$$\mu\Delta\vec{u}_f - \nabla p + \vec{f}_{\text{drag}} + \vec{f}_{\text{mem}} = 0, \quad (\text{S.10})$$

$$\nabla \cdot \vec{u}_f = 0, \quad (\text{S.11})$$

$$\vec{F}_e + \vec{F}_a + \vec{F}_{\text{drag}} + \vec{F}_{\text{adh}} + \vec{F}_{\text{net}}^{\text{attach}} = 0, \quad (\text{S.12})$$

$$\vec{F}_{\text{subs}} - \vec{F}_{\text{adh}} = 0. \quad (\text{S.13})$$

We will now describe the various forces which appear in Equations (S.10) to (S.12). The details of our framework and the methods that we use to discretize and simulate these equations can be found in [13].

S.2.2 Cytoskeletal Forces

Drag Force The cytoskeletal network moves with its own velocity field (\vec{U}_{net}) which is distinct from that of the viscous cytosol. The relative motion of these two materials gives rise to a drag force which acts upon the cytoskeleton

$$\vec{F}_{\text{drag}} = \xi \left(\vec{U}_f - \vec{U}_{\text{net}} \right), \quad (\text{S.14})$$

where $\vec{U}_f = \mathcal{S}^* \vec{u}_f$ is the fluid velocity evaluated on the cytoskeleton and ξ is a drag parameter which describes the mechanical coupling of the network and sol. There is necessarily an equal and opposite drag force which acts upon the fluid given by

$$\vec{f}_{\text{drag}} = -\mathcal{S} \vec{F}_{\text{drag}}. \quad (\text{S.15})$$

Elastic Forces The elastic force \vec{F}^e within the cytoskeleton is generated by the deformation of the cytoskeleton. We calculate \vec{F}^e using a discrete triangular network of nodes connected by springs. The strain energy in the elastic link connecting nodes \vec{X}_i and \vec{X}_j is given by

$$e_{ij} = \frac{k_{ij} dl_{ij}}{2} \left(\frac{|\vec{X}_i - \vec{X}_j| - dl_{ij}}{dl_{ij}} \right)^2, \quad (\text{S.16})$$

and we refer to this quantity as the *link energy*. Here, dl_{ij} is the length of the link in its undeformed state and the elastic parameter k_{ij} has units of force. The total elastic energy at a point \vec{X}_i is

$$E_i = \frac{1}{2} \sum_j e_{ij}, \quad (\text{S.17})$$

where it is understood that e_{ij} is zero unless \vec{X}_j is connected to \vec{X}_i . We refer to this E_i as the *node energy*. The factor of 1/2 which appears in (S.17) is included to ensure that summing the link energies or node energies over the network results in same total discrete elastic energy:

$$E = \sum_i E_i = \sum_{i,j} e_{ij}. \quad (\text{S.18})$$

From the form of (S.18) we compute the total force at a point \vec{X}_i as

$$\hat{F}_i = -\frac{\partial E}{\partial \vec{X}_i} = \sum_j -\frac{\partial e_{ij}}{\partial \vec{X}_i}, \quad (\text{S.19})$$

where the force exerted by the single elastic spring connecting nodes \vec{X}_i and \vec{X}_j is

$$-\frac{\partial e_{ij}}{\partial \vec{X}_i} = -k_{ij} \left(\frac{|\vec{X}_i - \vec{X}_j| - dl_{ij}}{dl_{ij}} \right) \frac{\vec{X}_i - \vec{X}_j}{|\vec{X}_i - \vec{X}_j|}. \quad (\text{S.20})$$

Finally, the force density at \vec{X}_i is given by

$$\vec{F}_i = \frac{\hat{F}_i}{dA_i}, \quad (\text{S.21})$$

where the area weight dA_i at each point \vec{X}_i is the sum of one third the area of each triangle with vertex \vec{X}_i . The elastic parameter for each link k_{ij} is chosen in such a way to that this network reproduces (for small strain) a two-dimensional linear, isotropic elastic solid with a given Lamé constant (λ_{2D})

$$k_{ij} = \frac{8\lambda_{2D}}{3dl_{ij}} \left(\frac{dA_i + dA_j}{2} \right). \quad (\text{S.22})$$

A detailed analysis of this procedure may be found in [13]. We then regard the stresses associated with this two-dimensional network as the integral (in the direction orthogonal to the substrate) of the stresses in a uniform three dimensional network (of height $d = 20 \mu\text{m}$) with the elastic modulus λ_E listed in Table S.1.

Dimensional Reduction To illustrate, consider a simplified elastic force balance law (in three dimensions) for the cytoskeleton. We disregard active stresses and lump everything but elastic forces into a term we call \vec{F}_{body} .

$$\vec{F}_{\text{body}} + \nabla \cdot \underline{\sigma} = 0. \quad (\text{S.23})$$

Here, $\underline{\sigma}$ is the elastic stress tensor and is proportional to some Lamé constant λ_E . Written out in component form, in the region $0 < z < d$, we have

$$\partial_x \sigma^{xx} + \partial_y \sigma^{yx} + \partial_z \sigma^{zx} + F_{\text{body}}^x = 0, \quad (\text{S.24})$$

$$\partial_x \sigma^{xy} + \partial_y \sigma^{yy} + \partial_z \sigma^{zy} + F_{\text{body}}^y = 0, \quad (\text{S.25})$$

$$\partial_x \sigma^{xz} + \partial_y \sigma^{yz} + \partial_z \sigma^{zz} + F_{\text{body}}^z = 0. \quad (\text{S.26})$$

We envision a *surface force* applied to the basal boundary of the cytoskeleton by adhesive structures linked to the substrate. This leads to a boundary condition on the force balance law

$$\underline{\sigma} \cdot \hat{z} = \vec{F}_{\text{bnd}} \text{ at } z = 0. \quad (\text{S.27})$$

Under the assumption that there is no network displacement in the z -direction, we may integrate in the z -direction to obtain

$$d \times \left(\partial_x \bar{\sigma}^{xx} + \partial_y \bar{\sigma}^{yx} + \bar{F}_{\text{body}}^x \right) + F_{\text{bnd}}^x = 0, \quad (\text{S.28})$$

$$d \times \left(\partial_x \bar{\sigma}^{xy} + \partial_y \bar{\sigma}^{yy} + \bar{F}_{\text{body}}^y \right) + F_{\text{bnd}}^y = 0, \quad (\text{S.29})$$

where the notation $\bar{\cdot}$ denotes the average over the z -direction. Equations (S.28) and (S.29) are equivalent to the two-dimensional vector equation

$$\nabla_{2D} \cdot (\underline{\sigma}_{2D}) + \vec{F}_{\text{body}}^{2D} + \vec{F}_{\text{bnd}}^{2D} = 0. \quad (\text{S.30})$$

Here, ∇_{2D} is the two-dimensional divergence, $\underline{\sigma}_{2D}$ is the two-dimensional stress, with units of *force per unit length*, $\vec{F}_{\text{body}}^{2D}$ is a two-dimensional body force, and $\vec{F}_{\text{bnd}}^{2D}$ is simply the projection of \vec{F} onto the xy -plane. Note that in Equation (S.27), \vec{F}_{bnd} represented a *surface force* applied to the boundary of the cytoskeleton. However, in the two-dimensional averaged model, this boundary force enters the force balance directly and is renamed to \vec{F}_{adh} . Finally, if $\underline{\sigma}$ is proportional to λ_E , then the two-dimensional stress $\underline{\sigma}_{2D}$ is proportional to

$$\lambda_{2D} = d \times \lambda_E, \quad (\text{S.31})$$

which also has units of force per unit length. For more details on this calculation, see [14]. A completely analogous formula is used to determine a two-dimensional drag parameter ξ_{2D} , given a the value of ξ listed in Table S.1. The drag parameter is discussed more in Section S.4

Note that the cell interior is modeled as a poroelastic material. It has been suggested that a poroelastic description of the cell interior is critical to properly capture cellular phenomenon driven by hydrodynamic pressure [15, 16].

Active Force The active term \vec{F}_a is the result of a prescribed traveling wave of contractile *force* in the individual links of the discrete network. The form of this is

$$\vec{F}_a = \frac{M}{2} \left(\cos \left(\frac{2\pi}{\ell_{\text{cont}}} x_{ij}^0 - \frac{2\pi}{T} t \right) + 1 \right) \hat{r}_{ij}, \quad (\text{S.32})$$

where x_{ij}^0 is the x -coordinate of the center of the link (in reference configuration) and \hat{r}_{ij} is the orientation unit vector of the link. This discretely approximates the *divergence* of the traveling wave of isotropic (two-dimensional) stress, of amplitude C , given in Section 3. The model parameter M and the amplitude of stress C are related by

$$C = \frac{3M}{2} \frac{\overline{d\ell}}{\overline{dA}}, \quad (\text{S.33})$$

where $\overline{d\ell}$ is the *average* length of the triangulation edges, and \overline{dA} is the average area of the faces in the triangulation. For more details, see [14]. Because the value of this term is chosen to produce the desired deformation amplitude, we simply report the force of contraction (M) in Table S.1.

Adhesion Forces We define a second Lagrangian structure which we refer to as the adhesive complexes. We denote the location of these adhesion complexes by \vec{X}_{adh} . We assume that each material point of the adhesive complexes is attached with the corresponding material point of the cytoskeleton via a Hookean elastic spring. The force density of this interaction *acting on the cytoskeleton* is given by

$$\vec{F}_{\text{adh}} = k_{\text{adh}} \left(\vec{X}_{\text{adh}} - \vec{X} \right). \quad (\text{S.34})$$

There is necessarily an equal and opposite force acting upon the adhesive complexes. The adhesive complexes are also subject to a force density due to interaction with the substrate. The precise nature of the proteins with which *physarum* adheres to the substrate is not known, though some candidates have been identified [17]. Regardless, the period of the deformations observed in

physarum is long (~ 100 sec) compared to the timescale of the dynamics of a cell-substrate bond. Over these long time scales and large ensembles of bonds, one can represent the dynamics of adhesion via a viscous drag law [18]. Therefore, we choose to model the the adhesive complex/substrate interaction via *modulated* viscous drag. The form of this interaction is given by

$$\vec{F}_{\text{subs}} = \zeta(\vec{x}, t) \left(\vec{U}_{\text{subs}} - \vec{U}_{\text{adh}} \right). \quad (\text{S.35})$$

The spatio-temporal form of ζ is a prescribed input of the model and is discussed in more detail in Section 3.

Membrane and Cortex We represent the membrane and cortex *together* as a single one dimensional structure which we refer to as the “membrane” for brevity. The membrane is described by its own Lagrangian coordinate θ , with domain Γ_{mem} , and its position is given by $\vec{X}_{\text{mem}}(\theta, t)$. We also define analogous spread and interpolation operators associated with the membrane (\mathcal{S}_{mem} and $\mathcal{S}_{\text{mem}}^*$). We note here that because the membrane is a lower dimensional structure, \vec{F}_{mem} has units of force per unit *length*. This is in contrast to \vec{F}_{drag} and other force densities which act upon the cytoskeletal network, which have units of force per unit area. The elastic force per unit length on the membrane (\vec{F}_{mem}^e) is assumed to be the result of tension within the membrane, which in turn is a function of the local strain. The elastic tension is given by

$$T = k_{\text{mem}} \frac{\left| \frac{\partial \vec{X}_{\text{mem}}}{\partial \theta} \right| - \left| \frac{\partial \vec{X}_0}{\partial \theta} \right|}{\left| \frac{\partial \vec{X}_0}{\partial \theta} \right|} + \gamma_{\text{mem}}. \quad (\text{S.36})$$

The first term in the tension penalizes deviations from a given reference configuration \vec{X}_0 , while the second term represents passive resting tension. The elastic force is calculated as the derivative of the tension within the membrane

$$\vec{F}_{\text{mem}}^e = \frac{\partial}{\partial \theta} (T\tau), \quad (\text{S.37})$$

where τ represents the unit tangent vector to the membrane. For a detailed description of the form of the tension within the membrane, see [12]. As before, the model parameters k_{mem} and γ_{mem} are chosen to reproduces the integral (orthogonal the substrate) of the tension that would result from a membrane with the elasticity (k) and resting tension (γ) which are listed in Table S.1. For details of this calculation, see [14].

The underlying cortex of *physarum* is mechanically coupled to the bulk cytoskeleton [19]. We model this coupling with a Hookean force law linking a material point on the membrane with the corresponding point on the boundary of the cytoskeleton. We assume that initially at time $t = 0$, the membrane configuration is equal to the reference configuration

$$\vec{X}_{\text{mem}}(\theta, 0) = \vec{X}_0(\theta). \quad (\text{S.38})$$

We further assume that this configuration coincides with the boundary of the elastic cytoskeletal network. Therefore, each material point θ is associated with a material point \vec{x} on the boundary of the network and

$$\vec{X}_{\text{mem}}(\theta, 0) = \vec{X}_{\text{net}}(\vec{x}_\theta, 0), \text{ for some } \vec{x}_\theta = \vec{x}_\theta(\theta). \quad (\text{S.39})$$

This generates a force density (per unit length) on the membrane, which is given by

$$\vec{F}_{\text{mem}}^{\text{attach}} = \kappa \left(\vec{X}_{\text{net}}(\vec{x}_\theta) - \vec{X}_{\text{mem}}(\theta) \right). \quad (\text{S.40})$$

There is necessarily an equal and opposite *boundary* force on the cytoskeletal network. We approximate this with a force per unit area supported on the exterior points of the cytoskeletal network ($[\vec{F}_{\text{net}}^{\text{attach}}]$). The parameter κ is chosen to prevent the membrane and the network from deviating by distances on the scale of the spacial discretization. The total force density acting on the membrane is the sum of elastic effects and the attachment to the cytoskeleton.

$$\vec{F}_{\text{mem}} = \vec{F}_{\text{mem}}^e + \vec{F}_{\text{mem}}^{\text{attach}}. \quad (\text{S.41})$$

Finally, we identify the membrane as a boundary within the fluid domain. Because the membrane is neutrally buoyant, all forces on the membrane are transmitted directly to the fluid. Again, this is accomplished via a spreading operator:

$$\vec{f}_{\text{mem}} = \mathcal{S}_{\text{mem}} \vec{F}_{\text{mem}}. \quad (\text{S.42})$$

On this boundary, we impose a no-slip boundary condition by stipulating that the membrane must move with the local fluid velocity [12].

Equations of Motion Derived from the force balance laws given by Equations (1) to (4), the equations of motion for the Lagrangian structures are

$$\frac{\partial \vec{X}_{\text{mem}}}{\partial t} = \mathcal{S}_{\text{mem}}^* \vec{u}_f, \quad (\text{S.43})$$

$$\frac{\partial \vec{X}_{\text{net}}}{\partial t} = \mathcal{S}^* \vec{u}_f + \frac{1}{\xi} \left(\vec{F}_e + \vec{F}_a + \vec{F}_{\text{adh}} + [\vec{F}_{\text{net}}^{\text{attach}}] \right), \quad (\text{S.44})$$

$$\frac{\partial \vec{X}_{\text{adh}}}{\partial t} = -\frac{\vec{F}_{\text{adh}}}{\zeta(\vec{x}, t)}. \quad (\text{S.45})$$

S.3 Model Parameters

We perform simulation of the model using the parameter values listed in Table S.1. Where possible, parameter values are chosen to be consistent with measured or estimated values in the literature. However, some model parameters are simply not experimentally measurable, and below we give a brief discussion of our estimates for these parameters.

The wavelength and period of the cytoskeletal contraction (ℓ_{cont} and T) are not directly measurable, but the wavelength and period of the resulting deformation are relatively straightforward to measure. We assume that the resulting deformation wave of the cell shape is directly correlated with the underlying cytoskeletal contraction. We choose $\ell_{\text{cont}} = 1.6$ mm (four body lengths) and $T = 100$ sec, which is consistent with the wavelength and period of deformation reported in [6] and in our own experiments.

The ratio of cytosol viscosity and drag coefficient (μ/ξ) is the Darcy permeability of the cytoskeleton. The permeability of the cytoskeleton has been estimated in the range of 10^{-5} – 10^{-3} μm^2 in other cell types [20, 21]. However, these estimates were based on dense actin networks (e.g. in lamellapodia), whereas *Physarum* pumps fluid through well formed flow channels relatively void of cytoskeletal meshwork (see Figure 2(a)). We estimate a permeability of 33.3 μm^2 in flow channels, however we do not use this value in our simulations. We model the cell interior as a uniform network with a single drag parameter of listed in Table S.1. This value is equivalent to a permeability of $\kappa = 3.28$ μm^2 , and was derived by homogenizing a non-uniform domain with a flow channel surrounded by a dense actin network. The details of this calculation are given in Section S.4.

The coefficient of specific adhesion A was chosen to range over values less than to much greater than the coefficient of nonspecific adhesion ϵ . The value of ϵ listed in Table S.1 was chosen to reproduce traction stresses of approximately the scale observed in the experiments.

Elastic moduli of living cells have been reported to vary over a vast range of values (10 Pa – 40 kPa) depending on cell type and experimental setup [22, 23, 24]. The elastic moduli of the cytoskeleton has been measured for *physarum*, but only for larger, more developed organisms; not the microplasmodia we consider in this work [25]. For this reason, we choose a moderate value of λ_E which falls well within the range of previously reported values. It has been previously observed that the posterior end of the cell is comprised of a much more developed actin cytoskeleton, while the anterior end of the cell exhibits much less dense intracellular structure [26]. For this reason, we assume that the front 20% of the model cell has an elastic modulus half as large as the posterior 80%. Similarly, the strength of contraction in this anterior region is half as strong to model the relatively lower capacity for contractile stress generation the less developed cytoskeleton.

Physarum plasmodia are known to be pressurized due to the contraction of the acto-myosin network of the cortex. In our model, the resting tension (γ) in the membrane/cortex gives rise to a resting fluid pressure within the cell. The value of γ listed in Table S.1 is chosen to produce a resting pressure of approximately 500 Pa. Based on our experiments, we estimate the intracellular resting pressure to be approximately the same size as the traction stresses (see Figure 2(b)). Micropipette experiments on other cell types have shown that inhibiting the contractility of cortical myosin can reduce the tension response of the membrane/cortex by more than 50% [27]. Without more reliable measurements of the elastic properties of *physarum* cortex, we chose the elastic parameter k to be slightly less than half the resting tension γ .

Table S.1: Model parameters for crawling simulation.

Parameter	Numerical Value	Description
L_x	400 μm	Cell Length
L_y	66.6 μm	Cell Width
μ	0.75 Pa sec	Cytosol Viscosity
ξ	2.29×10^{11} Pa sec/m ²	Drag Coefficient
λ_E	781 Pa	Cytoskeletal Elastic Modulus
M	120 pN	Amplitude of Active Contraction
k	10^{-2} N/m	Membrane/Cortex Elastic Stiffness
γ	1.6×10^{-2} N/m	Membrane Resting Tension
ϵ	2.29×10^6 Pa sec/m	Coefficient of Nonspecific Adhesion
A	$4.58 \times 10^4 - 2.29 \times 10^{10}$ Pa sec/m	Coefficient of Specific Adhesion
T	100 sec	Contraction Period
ℓ_{cont}	1600 μm	Contraction Wavelength

S.4 Permeability Bound

Permeability of cytoskeleton has been estimated in other cell types [20, 21]. However, these efforts have often focused on dense actin networks (for example, in lamellapodia of migrating keratocytes) and have produced low permeability values on the order of 10^{-5} – 10^{-3} μm^2 . We regard these estimates as something of a lower bound on reasonable values for the permeability in our model, because *Physarum* develops flow channels with relatively unformed cytoskeletal meshwork (see Fig. 2A). Under the assumption of a purely Newtonian cell interior (no cytoskeleton), it is possible to estimate an effective permeability which we regard as an upper bound of reasonable values for

our model. We note that the basal-dorsal thickness of *physarum* plasmodia in our preparation is approximately 20 μm , which is much less than the posterior-anterior length of the cell. Therefore, we make a thin gap approximation to arrive at the expression

$$\mu \frac{\partial^2 u}{\partial z^2} = -\frac{\partial p}{\partial x}, \quad (\text{S.46})$$

where z and x are the coordinates in the basal-dorsal and posterior-anterior directions respectively, u is the fluid velocity in the x direction, and p is the intracellular pressure. Assuming that the pressure is not a function of z , integrating, and imposing the no-slip boundary condition at $z = 0$ and $z = 20 \mu\text{m}$ allows us to derive the Darcy relation for the z -averaged flow

$$\mu \bar{u} = -\kappa_{\text{eff}} p_x, \quad (\text{S.47})$$

where the permeability $\kappa_{\text{eff}} = (20 \mu\text{m})^2/12 \approx 33.3 \mu\text{m}^2$. This may be interpreted as the effective permeability felt by the two-dimensional flow in the x - y plane. We note here that our model assumes a spatially homogeneous drag parameter, while the actual cell interior is heterogeneous. In fully formed flow channels, the permeability of the cell interior may range up to values suggested by the Newtonian approximation, while regions of dense cytoskeleton may exhibit permeabilities in line with those reported in lamellipodial actin networks. For this reason, we approximate a homogenized permeability through the whole cell body. We assume a cell width of h_{out} and that along the centerline of the cell, there exists a flow channel of width h_{in} . Within the flow channel, viscous effects are relevant, and the average fluid velocity profile obeys the equation

$$\mu \frac{\partial^2 \bar{u}}{\partial y^2} - \frac{\mu}{\kappa_{\text{eff}}} \bar{u} - p_x = 0. \quad (\text{S.48})$$

In the rest of the cell body, which is comprised of denser cortical actin meshwork, the fluid profile is assumed to obey the equation

$$\mu \bar{u} = \kappa_{\text{cort}} p_x. \quad (\text{S.49})$$

We solve both equations with a matching condition at the flow channel wall ($y = \pm h_{\text{in}}/2$) for the complete flow profile $\bar{u}(y)$. We then calculate the flux through a cross section of the cell due to the given pressure gradient p_x by

$$\bar{Q} = \int_{-\frac{h_{\text{out}}}{2}}^{\frac{h_{\text{out}}}{2}} \bar{u}(y) dy. \quad (\text{S.50})$$

Alternately, we calculate the flux due to a flow profile which results when we assume the entire cell interior is composed of a porous material with homogeneous permeability,

$$\tilde{Q} = \int_{-\frac{h_{\text{out}}}{2}}^{\frac{h_{\text{out}}}{2}} \tilde{u}(y) dy = - \int_{-\frac{h_{\text{out}}}{2}}^{\frac{h_{\text{out}}}{2}} \frac{\kappa_{\text{tot}}}{\mu} p_x dy. \quad (\text{S.51})$$

Finally, we equate \bar{Q} and \tilde{Q} and solve for the unknown homogenized permeability κ_{tot} . We have chosen the values of viscosity and cytoskeletal drag listed in Table S.1 to be consistent with a homogenized permeability of $\kappa_{\text{tot}} = 3.28 \mu\text{m}^2$. This resulted from assuming the parameter values listed in Table S.2.

Table S.2: Parameters for permeability homogenization.

Parameter	Numerical Value	Description
h_{out}	66.6 μm	Cell Width
h_{in}	17 μm	Flow Channel Width
κ_{eff}	33.3 μm^2	Effective Permeability In Flow Channel
κ_{cort}	10^{-4} μm^2	Cortical Permeability Outside Flow Channel

S.5 Random Substrate Generation

To generate random substrates for Section 4.6, we begin with a discretized Eulerian grid of size $Nx \times Ny$. On this grid, we can represent Fourier modes with wave numbers $k_x \in [-\lfloor Nx/2 \rfloor, \lfloor Nx/2 \rfloor]$, and $k_y \in [-\lfloor Ny/2 \rfloor, \lfloor Ny/2 \rfloor]$ in the x and y directions respectively. For each Fourier mode, we draw an angle $\theta(k_x, k_y)$ out of a uniform probability distribution on the interval $(0, 2\pi)$. These are done independently, with the exception of the constraint that

$$\theta(k_x, k_y) = \theta(-k_x, k_y) = \theta(k_x, -k_y). \quad (\text{S.52})$$

We then generate the function

$$\hat{h}(k_x, k_y) = e^{i\theta(k_x, k_y)}. \quad (\text{S.53})$$

The constraint on θ ensures that this may be interpreted as the randomly generated Fourier representation of a *real* valued function on our Eulerian grid. We then filter these Fourier modes via multiplication with the function

$$\hat{f}(k_x, k_y) = \frac{1}{\left(1 + \sqrt{k_x^2 + k_y^2}\right)^{1.5}}. \quad (\text{S.54})$$

After application of the filter, we define the function

$$\hat{g}(k_x, k_y) = \beta \hat{h} \hat{f}. \quad (\text{S.55})$$

Finally, we manually set the value

$$\hat{g}(0, 0) = \mu_r, \quad (\text{S.56})$$

and perform an inverse Fourier transform to generate the spatial heterogeneity $g(x, y)$. The parameter μ_r defines the mean of the function $g(x, y)$, while β controls its standard deviation. In practice, we found that a value of $\beta = 0.2$ resulted in a standard deviation of $\sigma_r = 0.34$ for our simulations.

S.6 Phase Velocity of Numerical Flow

We show here that the phase velocity of the intracellular flow observed in our numerical simulations does not depend meaningfully on the adhesion model. We calculate the phase velocity of the periodic flow wave in each numerical simulation, as we vary the coefficient of coordinated adhesion and phase parameter over the same ranges as in Section 4. The resulting values are illustrated in Figure S.2. For all simulations, the phase velocity falls between 24 and 38 $\mu\text{m}/\text{sec}$.

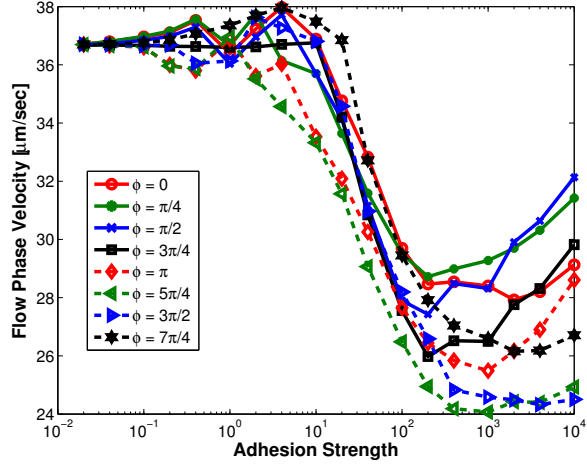


Figure S.2: Phase velocity of calculated intracellular flow as a function of adhesion strength.

S.7 Other Motility Modes

Below we illustrate the distinct motility modes that we observe in our experiments. Figure S.3(a) shows the flow and traction stress kymograph from a cell which robustly exhibits the peristaltic mode of motility. Figure S.3(b) shows the flow and traction stress kymograph from a cell which robustly exhibits the amphistaltic mode of motility. Figure S.3(c) shows the flow and traction stress kymograph from a cell which appears to switch from the amphistaltic to peristaltic mode during our observation. All traction stress kymographs are generated using the measured traction stresses with moving average removed.

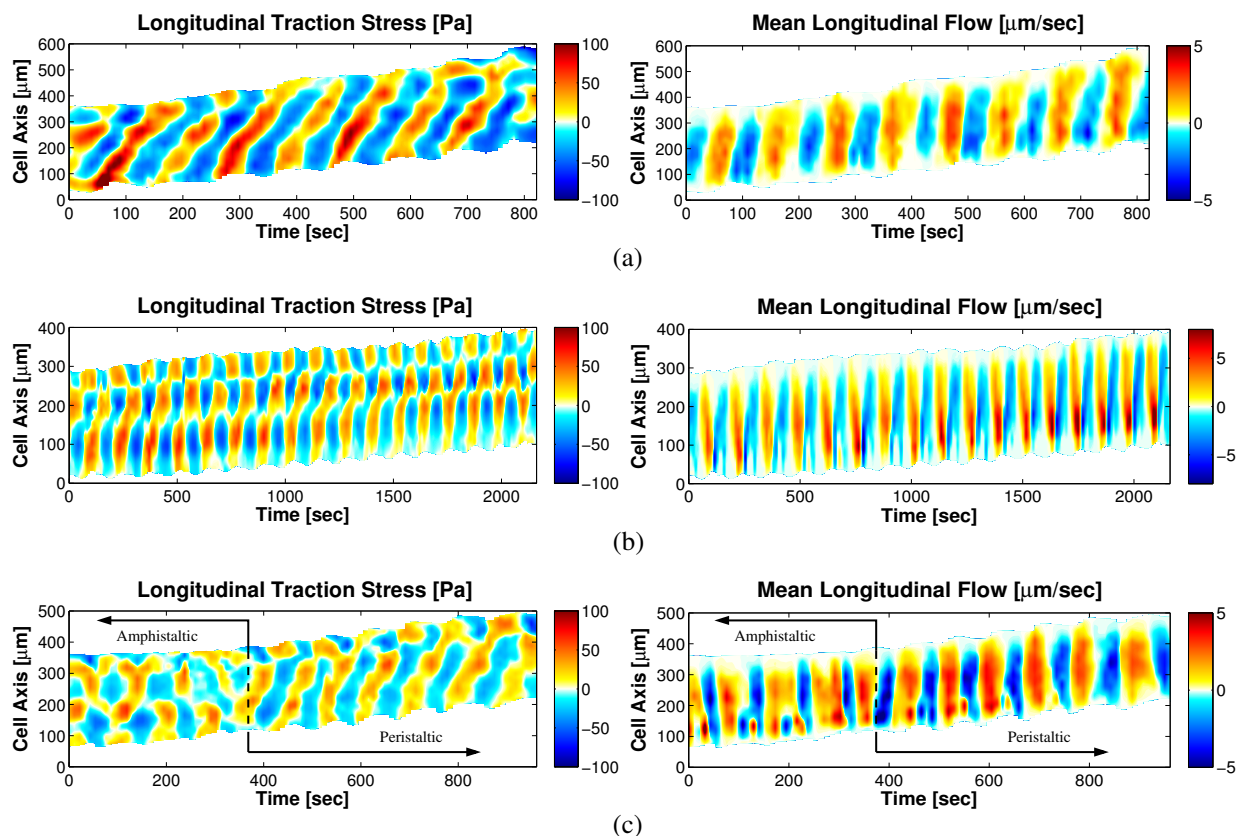


Figure S.3: (a) Flow and traction stress (with average removed) kymographs of *physarum* migrating using the peristaltic mode. (b) Flow and traction stress (with average removed) kymographs of *physarum* migrating using the amphistaltic mode. (c) Flow and traction stress (with average removed) kymographs of *physarum* migrating using both the amphistaltic and peristaltic modes.

References

- [1] Del Alamo, J. C., Meili, R., Alvarez-Gonzalez, B., Alonso-Latorre, B., Bastounis, E., Firtel, R. & Lasheras, J. C. 2013 Three-Dimensional Quantification of Cellular Traction Forces and Mechanosensing of Thin Substrata by Fourier Traction Force Microscopy. *PLoS ONE*, **8**, e69850.
- [2] Wang, Y. L. & Pelham, R. J. 1998 Preparation of a Flexible, Porous Polyacrylamide Substrate for Mechanical Studies of Cultured Cells. *Methods in Enzymology*, **298**, 489–496.
- [3] Engler, A., Bacakova, L., Newman, C., Hategan, A., Griffin, M. & Discher, D. 2004 Substrate Compliance Versus Ligand Density in Cell on Gel Responses. *Biophysical Journal*, **86**, 617–628.
- [4] Tse, J. R. & Engler, A. J. 2010 Preparation of Hydrogel Substrates with Tunable Mechanical Properties. *Current protocols in Cell Biology*, **Chapter 10**, 10.16.1–10.16.16.
- [5] Edelstein, A., Amodaj, N., Hoover, K., Vale, R. & Stuurman, N. 2010 Computer Control of Microscopes Using $\mu\text{Manager}$. *Current Protocols in Molecular Biology*, **Chapter 14**, 14.20.1–14.20.17.

- [6] Matsumoto, K., Takagi, S. & Nakagaki, T. 2008 Locomotive Mechanism of Physarum Plasmodia Based on Spatiotemporal Analysis of Protoplasmic Streaming. *Biophysical Journal*, **94**, 2492–2504.
- [7] Lewis, O., Zhang, S., Guy, R. D. & Del Álamo, J. C. 2014. Traction Force Microscopy and Particle Image Velocimetry of Migrating Physarum. <http://dx.doi.org/10.6084/m9.figshare.1267558>.
- [8] Willert, C. E. & Gharib, M. 1991 Digital Particle Image Velocimetry. *Experiments in Fluids*, **10**, 181–193.
- [9] Del Alamo, J. C., Meili, R., Alonso-Latorre, B., Rodriguez-Rodriguez, J., Aliseda, A., Firtel, R. A. & Lasheras, J. C. 2007 Spatio-Temporal Analysis of Eukaryotic Cell Motility by Improved Force Cytometry. *Proceedings of the National Academy of Sciences*, **104**, 13343–13348.
- [10] Peskin, C. S. 1977 Numerical Analysis of Blood Flow in the Heart. *Journal of Computational Physics*, **25**, 220–252.
- [11] Mittal, R. & Iaccarino, G. 2005 Immersed Boundary Methods. *Annual Review of Fluid Mechanics*, **37**, 239–261.
- [12] Peskin, C. S. 2002 The Immersed Boundary Method. *Acta Numerica*, **11**, 479–517.
- [13] Strychalski, W., Copos, C. A., Lewis, O. L. & Guy, R. D. 2015 A Poroelastic Immersed Boundary Method with Applications to Cell Biology. *Journal of Computational Physics*, **282**, 77 – 97.
- [14] Lewis, O. L. 2014 Mathematical Investigation of Hydrodynamic Contributions to Amoeboid Cell Motility in Physarum polycephalum. Ph.D. thesis, University of California Davis.
- [15] Charras, G. T., Mitchison, T. J. & Mahadevan, L. 2009 Animal Cell Hydraulics. *Journal of Cell Science*, **122**, 3233–3241.
- [16] Moeendarbary, E., Valon, L., Fritzsche, M., Harris, A. R., Moulding, D. A., Thrasher, A. J., Stride, E., Mahadevan, L. & Charras, G. T. 2013 The Cytoplasm of Living Cells Behaves as a Poroelastic Material. *Nature Materials*, **12**, 253–261.
- [17] Hayase, M., Maekawa, A., Yubisui, T. & Minami, Y. 2008 Properties, Intracellular Localization, and Stage-Specific Expression of Membrane-Bound Beta-Glucosidase, BglM1, From Physarum Polycephalum. *The International Journal of Biochemistry & Cell Biology*, **40**, 2141–2150.
- [18] Srinivasan, M. & Walcott, S. 2009 Binding Site Models of Friction Due to the Formation and Rupture of Bonds: State-Function Formalism, Force-Velocity Relations, Response to Slip Velocity Transients, and Slip Stability. *Physical Review E*, **80**, 046124.
- [19] Brix, K. & Stockem, W. 1987 Studies on Microplasmodia of Physarum polycephalum. *Cell Biology International Reports*, **11**, 529–536.
- [20] Keren, K., Yam, P. T., Kinkhabwala, A., Mogilner, A. & Theriot, J. A. 2009 Intracellular Fluid Flow in Rapidly Moving Cells. *Nature Cell Biology*, **11**, 1219–1224.
- [21] Charras, G. T., Yarrow, J. C., Horton, M. A., Mahadevan, L. & Mitchison, T. J. 2005 Non-Equilibration of Hydrostatic Pressure in Blebbing Cells. *Nature*, **435**, 365–369.

- [22] Yamada, S., Wirtz, D. & Kuo, S. C. 2000 Mechanics of Living Cells Measured by Laser Tracking Microrheology. *Biophysical Journal*, **78**, 1736–1747.
- [23] Bausch, A. R., Ziemann, F., Boulbitch, A. A., Jacobson, K. & Sackmann, E. 1998 Local Measurements of Viscoelastic Parameters of Adherent Cell Surfaces by Magnetic Bead Microrheometry. *Biophysical Journal*, **75**, 2038–2049.
- [24] Wang, N., Butler, J. P. & Ingber, D. E. 1993 Mechanotransduction Across the Cell Surface and Through the Cytoskeleton. *Science*, **260**, 1124–1127.
- [25] Norris, C. H. 1940 Elasticity Studies on the Myxomycete, *Physarum Polycephalum*. *Journal of Cellular and Comparative Physiology*, **16**, 313–322.
- [26] Stockem, W. & Brix, K. 1994 Analysis of Microfilament Organization and Contractile Activities in *Physarum*. *International Review of Cytology - A Survey of Cell Biology*, **149**, 145–215.
- [27] Tinevez, J.-Y., Schulze, U., Salbreux, G., Roensch, J., Joanny, J. F. & Paluch, E. 2009 Role of Cortical Tension in Bleb Growth. *Proceedings of the National Academy of Sciences*, **106**, 18581–18586.